Micro and Nanostructures 210 (2026) 208482

Contents lists available at ScienceDirect

Micro and Nanostructures

journal homepage: www.journals.elsevier.com/micro-and-nanostructures

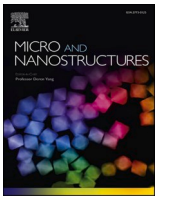

Impact of optical and recombination losses on the photovoltaic parameters of thin-film solar cells with *n*-CdS(ZnO, ZnMgO)/*p*-$Cu_{12}Sb_4S_{13}$ heterojunctions

Artem Zabuha [a,*], Oleksandr Dobrozhan [a], Dmytro Velykodnyi [b], Anatoliy Opanasyuk [a]

[a] Department of Electronics and Computer Technology, Sumy State University, 40007, Sumy, Ukraine
[b] Department of Computer Science, Sumy State University, 40007, Sumy, Ukraine

ARTICLE INFO

Keywords:
Solar cells
Tetrahedrite
Optical losses
Recombination losses
Short-circuit current density

ABSTRACT

Despite the favorable material properties of tetrahedrite, thin-film solar cells based on it exhibit low efficiencies (<1.5 %) due to significant optical and recombination energy losses. In this work, the influence of these losses on the photovoltaic parameters of solar cells with *n*-CdS(ZnO, ZnMgO)/*p*-$Cu_{12}Sb_4S_{13}$ heterojunctions and *n*-ITO front conductive contacts was analyzed. The *n*-ZnO window layer demonstrated superior spectral transparency (T = 93.3 %). Optical and recombination losses were found to decrease J_{sc} of such devices by 20–41 %. The optimized design of the *n*-ZnMgO/*p*-$Cu_{12}Sb_4S_{13}$ solar cell (d_{ZMO} = 25 nm, d_{ITO} = 100 nm), with an acceptor concentration in the absorbing layer of $N_a = 10^{16}$ cm^{-3}, achieved the highest values of J_{sc} (~22.7 mA/cm^2) and power conversion efficiency η (~19.9 %), due to enhanced band alignment with the *p*-$Cu_{12}Sb_4S_{13}$ layer and reduced recombination losses. Based on these findings, practical recommendations are provided for the fabrication of high-efficiency solar cells utilizing a $Cu_{12}Sb_4S_{13}$ absorbing layer.

1. Introduction

By the middle of the 21st century, solar energy is expected to become the predominant source of electricity for humanity [1]. According to projections, global annual electricity generation from solar power may reach approximately 400 TWh by 2030 [2]. At present, most commercial solar cells (SCs) are based on monocrystalline, polycrystalline, and amorphous silicon technologies, which belong to the first generation [3]. Alongside them, cost-effective thin-film SCs, classified as second-generation, are actively being developed using chalcogenide semiconductors such as $CuIn_{1-x}Ga_xSe_2$ (CIGS), III–V group compounds (GaAs, InP), and II–VI group compounds (CdTe) [4]. Moreover, organic photovoltaic devices have emerged as promising SCs, offering flexibility and recyclability [5].

Currently, first- and second-generation SC are highly optimized, with efficiencies up to 27.3 % (Si), 23.4 % (CIGS), 29.1 % (GaAs), 24.2 % (InP), and 21.0 % (CdTe) [3], approaching the Shockley–Queisser limit of 28–32 % [6] and highlighting the maturity of these technologies. Nevertheless, the large-scale deployment of these materials is constrained by the limited availability of critical elements such as tellurium (Te) and indium (In), as well as the environmental and health hazards associated with cadmium (Cd) and selenium

* Corresponding author. 116, Kharkivska st., 40007, Sumy, Ukraine.
E-mail address: artem.zabuha@student.sumdu.edu.ua (A. Zabuha).

https://doi.org/10.1016/j.micrna.2025.208482
Received 6 June 2025; Received in revised form 1 November 2025; Accepted 21 November 2025
Available online 21 November 2025

(Se).

In recent years, multicomponent compounds such as Cu_2ZnSnS_4 (CZTS), $Cu_2ZnSnSe_4$ (CZTSe), and their solid solutions of $Cu_2ZnSn(S_{1-x}Se_x)_4$ (CZTSSe) have been explored as alternative absorbing layer materials for third-generation SCs. Experimental efficiencies remain modest (~10.0 % for CZTS, 13.5 % for CZTSSe [7]) due to the structural complexity of kesterite materials, the formation of secondary phases, and challenges in controlling native point defects [8]. Developing new, more efficient, and structurally simpler absorbing materials remains a key objective for the next-generation photovoltaics.

A promising candidate for third-generation photovoltaic absorbing material is the tetrahedrite $Cu_{12}Sb_4S_{13}$ (CAS). It consists of non-toxic, earth-abundant elements and behaves as a degenerate *p*-type semiconductor with an ultra-high hole concentration [9]. According to Ref. [10], planar triangular sites in CAS are occupied by Cu^+ ions, while tetrahedral sites are shared by Cu^+/Cu^{2+} with an average oxidation state of +1.33, resulting in four holes per unit cell (concentration of $\sim 3.6 \times 10^{21}$ cm^{-3} purely from structural considerations). The material exhibits a high light absorption coefficient ($\alpha \sim 10^4$ cm^{-1}), independent of the film preparation method. According to Ref. [9], the films had very low resistivity ($\rho \sim$ 0.001–0.004 Ohm·cm), and a Fermi level about 0.12 eV below E_v, confirming its degenerate *p*-type nature. When doped with Zn or Se, CAS becomes a non-degenerate semiconductor with an exceptionally high absorption coefficient ($\alpha \approx 10^5$ cm^{-1}), enabling ultrathin (hundreds of nm) absorbing layers suitable for transparent and flexible SCs. While CAS has been extensively studied for thermoelectric applications [11], its viability as an absorbing layer material remains less explored. Its electronic properties are highly tunable: depending on copper content, the bandgap (E_g) can vary between 1.1 and 1.9 eV [12–14], with either direct or indirect electronic transitions, making it a promising material for efficient solar energy conversion.

Cadmium sulfide (CdS), with a bandgap of $E_g = 2.42$ eV, is still the dominant window layer in thin-film photovoltaics [15]. However, wider-bandgap alternatives such as ZnSe ($E_g = 2.67$ eV) [15], ZnS ($E_g = 3.68$ eV) [15], SnS_2 ($E_g = 2.18$–3.38 eV) [16], ZnO ($E_g = 3.37$ eV) [17], and $Zn_{1-x}Mg_xO$ (ZMO, $E_g \approx 4.0$ eV at $x = 0.3$) [18], are being explored as substitutes. ZnO stands out due to its low cost, environmental friendliness, and highly tunable optical and electrical properties via Mg doping, which can be precisely tuned during material growth [19,20].

A literature review reveals that the efficiency of real thin-film SCs with CAS absorbing layers does not exceed ~1.5 % [21], mainly due to energy loss mechanisms during photovoltaic conversion [22]. The main irreversible loss channels in SCs include: (i) reflection of incident light from the device surface and internal interfaces; (ii) transmission of unabsorbed radiation through the device; (iii) parasitic absorption in non-active auxiliary layers; (iv) recombination of photogenerated electron-hole pairs at surfaces and within bulk regions. Enhancing the efficiency of SCs critically depends on minimizing these losses through careful structural design and improved quality of each functional layer.

In our previous studies, using modelling approaches, we optimized several SCs structures, including: glass/ITO/ZnS(SnS_2)/SnS [23], glass/ITO(ZnO:Al)/ZnMgO/SnS [24], glass/ITO(ZnO:Al)/ZnMgO/CuO(Cu_2O) [25,26], glass/ITO(ZnO)/CdS(ZnSe, ZnS)/CZTS [15], and glass/ITO(ZnO:Al)/CdS/CZTSSe [27]. Building upon this experience, the present work, for the first time, focuses on studying optical and recombination losses in the SCs with the *n*-CdS(ZnO, ZnMgO)/*p*-$Cu_{12}Sb_4S_{13}$ heterojunctions, applying ITO as the front current-collecting contact.

2. Theory and calculation

Modeling is a key step toward the development of efficient SCs. For example, the authors in Refs. [28,29] compared simulation results with experimental parameters, identifying the critical factors influencing the performance of actual SCs. In Ref. [30], the SCAPS-1D software was used to optimize the layer thicknesses of SC, and the reliability of the simulation results was validated experimentally. Modeling further allows assessing the interfacial defect density [28] and the impact of series and shunt resistances [31] on the main characteristics of SCs. In our case, the modeling employed analytical expressions based on the continuity equation, incorporating factors that determine the quantum efficiency, together with the Sah–Noyce–Shockley theory to account for recombination processes in the space charge region (SCR). These expressions also form the basis of the SCAPS software package for simulating the key parameters of SCs. The absorptivity of CAS is assessed using the Bouguer–Lambert–Beer law, and reflectance is calculated from Fresnel equations. The width of the SCR is determined from Poisson's equation. Solving the continuity equation enables the determination of the diffusion and drift contributions to the internal quantum efficiency of the device. As a result, we identified a SC design with the highest efficiency and provided recommendations for the development of efficient devices based on CAS absorbing layers.

According to the Shockley–Queisser limit, the maximum efficiency of a single-junction SC depends on the bandgap energy of the absorbing layer. A comparison of the theoretical efficiency of photovoltaic devices based on materials with a bandgap close to that of CAS under AM 1.5G illumination is presented in Table 1. These values are standard and widely cited in the literature [32].

Table 1
The maximum theoretical efficiency of SCs with absorbing layers of materials with bandgaps similar to CAS.

Material	Bandgap width	Maximum theoretical efficiency (Shockley–Queisser)
CZTS	1.5 eV	~30 %
CZTSSe	1.0–1.5 eV	~33 %
$CuSbS_2$	1.4–1.7 eV	~23 %
CAS	1.1–1.9 eV	~32 %
CdTe	1.5 eV	~30 %

In this study CAS tetrahedrite is proposed as the absorbing layer in thin-film SCs. This material satisfies all the key criteria for absorbing layers in third-generation SC, including elemental abundance, non-toxicity, and favorable optoelectronic properties [33]. One of the fundamental characteristics required for modelling optical and recombination losses, as well as for predicting the photovoltaic parameters of the SC, is the material's absorptivity (A). According to Ref. [34], it is essential to distinguish between the solar absorptivity (A_{sr}) and the absorptivity of the photon flux (A_{hv}). Notably, these parameters have not yet been quantified for CAS materials. This work presents a calculation of both A_{sr} and A_{hv}.

Under conditions of normal light incidence, the solar absorptivity is calculated using the Bouguer–Lambert law [35]:

$$A_{sr}(d) = \frac{\sum_i^{\frac{E_i+E_{i-1}}{2}} \left[1 - e^{\left(-\frac{\alpha_i+\alpha_{i-1}}{2}\right)d}\right] \Delta\lambda_i}{\sum_i^{\frac{E_i+E_{i-1}}{2}} \Delta\lambda_i}, \quad (1)$$

where, E_i – solar spectral irradiance under AM 1.5G illumination conditions; α_i – light absorption coefficient at wavelength λ_i; d – thickness of the absorbing layer; $\Delta\lambda_i$ – interval between adjacent wavelengths in the ISO 9845–1:2022.

The solar spectral irradiance (E) under AM 1.5G conditions, which is essential for subsequent calculations, is presented in Fig. 1. The data used to construct this curve were sourced from the ISO 9845–1:2022 standard [36].

Additionally, Fig. 1 illustrates the wavelength-dependent absorption coefficient (α) of the CAS, as reported in Ref. [37]. The calculations were carried out for wavelengths ranging from 300 nm, below which solar irradiance is effectively negligible at the Earth's surface, to 1000 nm, corresponding to the CAS minimum bandgap energy ($E_g \approx 1.1$ eV) [13].

It is well established that the semiconductor material efficiently absorbs photons with energy exceeding the bandgap E_g. The inter- and extrapolation of the E_i and α values was performed using OriginPro: Data Analysis and Graphing Software, since the reference data provide their values at different wavelengths, whereas equation (1) requires these parameters to correspond to the same wavelength λ.

It is also important to note that the generation of electron-hole pairs in the absorbing material is not directly proportional to the incident solar irradiance. This is because electron-hole pair formation occurs for photon energies greater than E_g, regardless of the exact photon energy. Also, at small layer thicknesses, the material mainly absorbs lower-energy photons, while the absorption of higher-energy photons increases with the layer thickness. Thus, accurate calculation of the photon flux absorptivity (A_{hv}) is crucial.

To this end, the following relation was used:

$$A_{hv}(d) = \frac{\sum_i^{\frac{E_i+E_{i-1}}{2h\nu_i}} \left[1 - e^{\left(-\frac{\alpha_i+\alpha_{i-1}}{2}\right)d}\right] \Delta\lambda_i}{\sum_i^{\frac{E_i+E_{i-1}}{2h\nu_i}} \Delta\lambda_i}, \quad (2)$$

where, $h\nu$ – the photon energy.

To convert solar energy into electricity, thin-film SC with either a "substrate" or "superstrate" configurations are commonly employed [38]. Among these, converters with the "superstrate" design are generally considered more efficient, which is why this architecture was selected for modelling the physical processes in the photovoltaic converters. Thin-film SCs based on heterojunctions with a "superstrate" structure feature a multilayer configuration comprising a substrate (glass), a front current collector (ITO), a window layer (CdS, ZnO, or ZMO), and an absorbing layer (CAS), along with a rear metal contact that ensures ohmic contact with the latter. The solar cell structure used for modelling is illustrated in Fig. 2.

The methodology for calculating optical and recombination energy losses was previously validated for structures with CdTe and

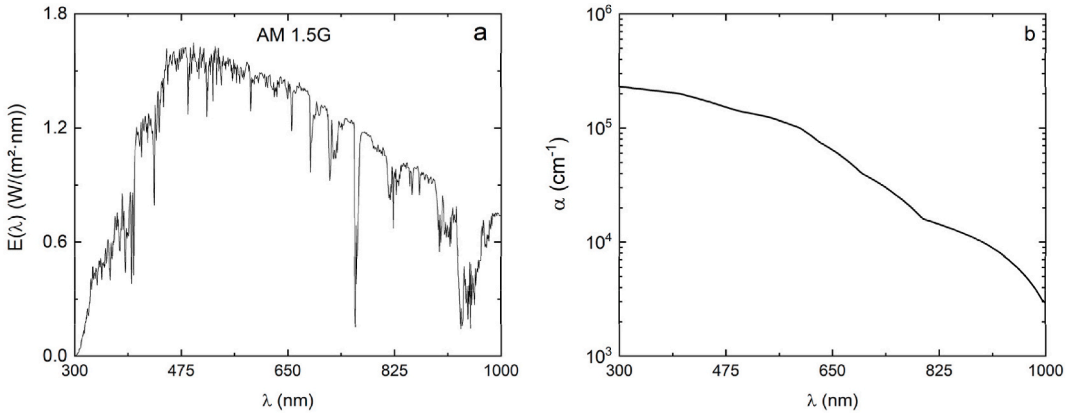

Fig. 1. Spectral dependency of (a) solar irradiance (E) under AM 1.5G conditions and (b) CAS absorption coefficient (α) taken from the literature [37].

CZTS absorbing layers [39]. In this work, the approach has been adapted to novel material – CAS. The path of sunlight through the solar cell involves transmission across auxiliary layers: substrate (glass), charge collective layer (ITO), and window layer (CdS, ZnO, or ZMO). During this process, optical energy losses occur due to both reflection at multiple interfaces (air-glass, glass-ITO, ITO-(CdS, ZnO, ZMO), and (CdS, ZnO, ZMO)-CAS) and photon absorption within the auxiliary layers [15].

We modeled the light reflection processes within the multilayer device structure, varying the thickness of the window layer from 25 to 100 nm and the current-collecting layer thickness from 100 to 200 nm. This thickness range corresponds to typical values observed in practical photovoltaic converters based on the studied materials [15].

The reflection at the interfaces between layers was calculated by the Fresnel equation [40]:

$$R = \left(\frac{n_i - n_j}{n_i + n_j}\right)^2, \tag{3}$$

where, n_i, n_j –the refractive indices of the two contacting materials.

When conductive materials are used in solar cell structures, the reflection coefficient is calculated using the following relation [40]:

$$R_{ij} = \frac{\left|n_i^* - n_j^*\right|}{\left|n_i^* + n_j^*\right|} = \frac{(n_i - n_j)^2 + (k_i - k_j)^2}{(n_i + n_j)^2 + (k_i + k_j)^2}, \tag{4}$$

where, n_i^*, n_j^* – complex refractive indices; k_i, k_j – extinction (attenuation) coefficients.

The spectral dependencies of the refractive index (n) and extinction coefficient (k) for each layer of the solar cell are presented in Fig. 3. The extinction coefficient of glass is assumed to be zero ($k = 0$), as specialized glass with minimal absorption in the relevant spectral range is typically employed in SC [41].

To determine the refractive index of glass, the Sellmeier equation was applied [40]:

$$n^2 = 1 + \frac{a_1\lambda^2}{\lambda^2 - \lambda_1^2} + \frac{a_2\lambda^2}{\lambda^2 - \lambda_2^2} + \frac{a_3\lambda^2}{\lambda^2 - \lambda_3^2}, \tag{5}$$

where, $a_1 = 0.6962$, $a_2 = 0.4079$, $a_3 = 0.8974$, $\lambda_1 = 68$ nm, $\lambda_2 = 116$ nm, $\lambda_3 = 9896$ nm.

To build the spectral dependencies of the refractive index (n) and extinction coefficient (k), the optical constants of ITO, CdS, ZnO, and ZMO were taken from Refs. [25,42–44]. For air, the modelling was performed using the standard assumptions: $n_1 = 1$ and $k_1 = 0$.

In the case of the CAS material, the values of n and k were derived from the corresponding spectral dependencies of the absorption and reflection coefficients, as reported in Refs. [9,37].

The transmission of light through the auxiliary layers of the solar cell (glass, ITO, CdS, ZnO, ZMO) can be approximated using the relation $T = 1 - R$, assuming negligible absorption within these layers. Accordingly, the transmission coefficients of the multilayer structure were calculated using the following relation [41]:

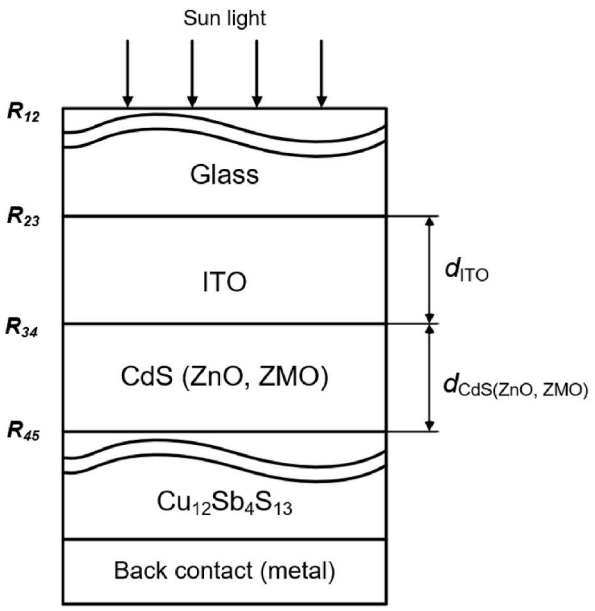

Fig. 2. Structure of solar cell with n-CdS(ZnO, ZMO)/p-$Cu_{12}Sb_4S_{13}$ heterojunctions (R_{ij} – coefficients of reflection from the boundaries, d_i – thickness of the window and current-collecting layer).

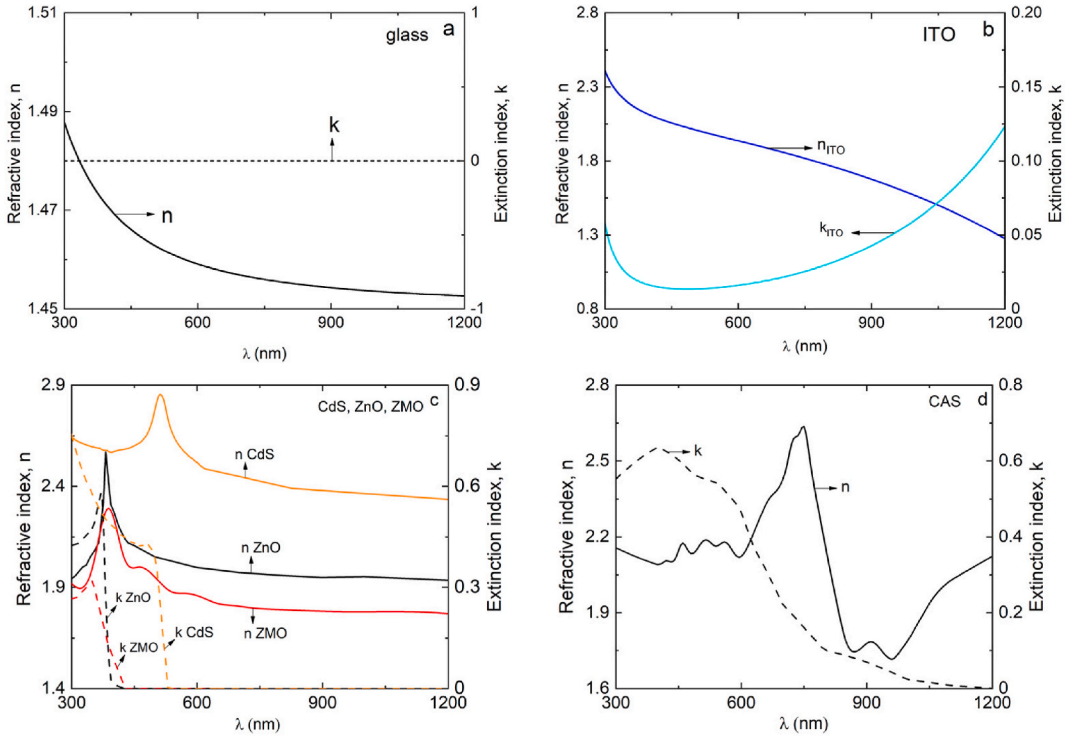

Fig. 3. Spectral dependencies of refractive indices (n) and extinction coefficients (k) for (a) glass, (b) ITO, (c) (CdS, ZnO, ZMO), and (d) CAS materials.

$$T(\lambda) = (1 - R_{12})(1 - R_{23})(1 - R_{34})(1 - R_{45}), \tag{6}$$

where, R_{12}, R_{23}, R_{34}, R_{45} – the light reflection coefficients at the interfacial boundaries: air-glass, glass-ITO, ITO-(CdS, ZnO, ZMO), and (CdS, ZnO, ZMO)-CAS.

To determine the optimal structure of the solar cell, the optical loss coefficient (Δ) within the device was calculated using the following equation:

$$\Delta = \frac{T_{\max}(\lambda) - (1/n)\sum_{i=1}^{n} T_i(\lambda)}{T_{\max}(\lambda)}. \tag{7}$$

Since $T_{\max} = 1$, expression (7) can be simplified to the form:

$$\Delta = 1 - \frac{1}{n}\sum_{i=1}^{n} T_i(\lambda). \tag{8}$$

In the general case, when evaluating the light transmission through the auxiliary layers (ITO, CdS, ZnO, ZMO), it is also necessary to account for light losses due to its absorption.

The transmittance of a multilayer structure, accounting for both reflection and absorption losses in the front and window layers, can be calculated using the following equation [41]:

$$T(\lambda) = (1 - R_{12})(1 - R_{23})(1 - R_{34})(1 - R_{45})\left(e^{-\alpha_1 d_1}\right)\left(e^{-\alpha_2 d_2}\right), \tag{9}$$

where, α_1, α_2 – the absorption coefficients of the materials of the conductive and window layers; d_1, d_2 – thicknesses of the conductive and window layers.

The absorption coefficient $\alpha(\lambda)$, considering the wavelength-dependent extinction coefficient $k(\lambda)$, is determined by the relation:

$$\alpha(\lambda) = \frac{4\pi}{\lambda}k. \tag{10}$$

A key parameter determining the efficiency of a solar cell is the internal quantum yield (Q_{int}). It is defined as the ratio of the number of electron-hole pairs generated by absorbed photons to the total number of incident photons reaching the absorbing layer and contributing to the drift (J_{drift}) and diffusion (J_{dif}) components of the short-circuit current density (J_{sc}).

The Q_{int} of the solar cell depends on recombination losses occurring at the n-CdS(ZnO, ZMO)/p-CAS interfaces, within the bulk and

rear surface of the CAS absorbing layer, as well as in the bulk of the window layers (CdS, ZnO, ZMO). In addition, it is important to evaluate the external quantum yield (Q_{ext}), which reflects optical losses due to reflection and parasitic absorption in the auxiliary layers of the device [45,46].

One of the critical parameters for analyzing recombination losses in SC is the width of the SCR (denoted as w), depletion region of the heterojunction where the built-in electric field separates photogenerated electron-hole pairs. This width primarily depends on the concentration difference of uncompensated acceptors and donors ($N_A - N_D$) and the height of the contact barrier (V_D) at the heterointerface [15]. However, the value of the contact barrier for the studied heterojunctions is unknown. Thus, energy band diagrams of the n-CdS(ZnO, ZMO)/p-CAS were constructed with the physical parameters presented in Table 2.

The offsets between the conduction band (ΔE_c) and valence band (ΔE_v) for the n-CdS(ZnO, ZMO)/p-CAS heterojunctions was determined using the expressions:

$$\Delta E_c = \chi_{CAS} - \chi_{CdS,ZnO,ZMO} \tag{11}$$

$$\Delta E_v = \left(\chi_{CdS,ZnO,ZMO} + E_{g\ CdS,ZnO,ZMO}\right) - \left(\chi_{CAS} + E_{gCAS}\right) = E_{g\ CdS,ZnO,ZMO} - E_{g\ CAS} - \Delta E_c. \tag{12}$$

The total contact potential (V_D) at the heterojunctions is determined by the difference in work functions of the materials forming the junction is given by the expression:

$$V_D = V_{CAS} + V_{CdS,ZnO,ZMO} = W_{CAS} - W_{CdS,ZnO,ZMO}. \tag{13}$$

The ratio of the potentials $V_{(CdS,ZnO,ZMO)}$ and V_{CAS} is given by the expression:

$$\frac{V_{CdS,ZnO,ZMO}}{V_{CAS}} = \frac{N_{A\ CAS} \cdot \varepsilon_{CAS}}{N_{D\ CdS,ZnO,ZMO} \cdot \varepsilon_{CdS,ZnO,ZMO}}, \tag{14}$$

where, $N_{A\ CAS}$, $N_{D\ CdS,ZnO,ZMO}$ – the concentrations of uncompensated donors and acceptors.

In contrast to n-CdS/p-CdTe heterojunctions, where current transport resembles that of a Schottky diode [49], such a model is not suitable for n-CdS(ZnO, ZMO)/p-CAS structures. This is due to the high carrier concentration in the CAS absorbing layer ($N_A = 10^{18}$–10^{21} cm^{-3} [50]), which significantly exceeds the acceptor concentration in CdTe ($N_A = 10^{14}$–10^{17} cm^{-3} [46]) and can also surpass the donor concentration in the window layers ($N_D = 10^{16}$–10^{18} cm^{-3}). However, the carrier concentration in CAS can be reduced by substituting Cu with Zn^{2+} or Mn^{2+}.

As a result, the space charge region extends into both the window layer (w_n) and the absorbing layer (w_p), and their widths are described by the following expressions [51]:

$$w_n = \sqrt{\frac{2\varepsilon_n\varepsilon_p\varepsilon_0(V_D - qU)}{qN_D{}^2\left(\varepsilon_p/N_A + \varepsilon_n/N_D\right)}}, w_p = \sqrt{\frac{2\varepsilon_n\varepsilon_p\varepsilon_0(V_D - qU)}{qN_A{}^2\left(\varepsilon_p/N_A + \varepsilon_n/N_D\right)}}, \tag{15}$$

$$w = \sqrt{\frac{2\varepsilon_n\varepsilon_p\varepsilon_0(V_D - qU)}{q}\left(\frac{1}{\varepsilon_n N_D} + \frac{1}{\varepsilon_p N_A}\right)}, \tag{16}$$

where, ε_n, ε_p –permittivity of the window and absorbing layer; ε_0 – permittivity of vacuum; $V_D = qV_{bi}$ – height of the contact barrier (V_{bi} – built-in potential); U – applied external voltage; q – electron charge; N_A, N_D – concentration of uncompensated acceptors and donors.

To evaluate w and Q_{int}, the physical parameters listed in Table 3 were used. As shown in Refs. [45,46], solving the continuity equation enables estimation of the drift component of the internal quantum efficiency (Q_{drift}). This component accounts for carrier recombination at the heterointerface and within the SCR, and can be represented as the difference of two contributions (see Appendix 1, Eq. (A.1) for details):

$$Q_{drift\ p(n)} = A - B$$

The A contribution describes the collection of carriers generated within the depletion region, where a strong electric field is present.

Table 2
The physical parameters of the materials used to build the band energy diagrams and calculate the contact barrier height for the n-CdS(ZnO, ZMO)/p-CAS [12,15,17,18,44,47,48].

Parameter	n-CdS	n-ZnO	n-ZMO	p-CAS
E_g, eV	2.42	3.40	4.00	1.70
χ, eV	4.50	4.10	3.10	3.07
E_F, eV	0.04	0.27	0.28	0.21
W, eV	4.54	4.37	3.38	4.56
ε	10.2	10.8	8.7	8.1
N_A, cm^{-3}	–	–	–	10^{14}–10^{17}
N_D, cm^{-3}	10^{15}–10^{17}	10^{15}–10^{17}	10^{15}–10^{17}	–

Table 3
The values of the parameters required for calculating w and Q [9,12,43,52–54].

Parameter	Value
V_D, eV	$(0.02)_{CdS}$, $(0.19)_{ZnO}$, $(1.18)_{ZMO}$
S, S_b, cm/s	10^7
$\tau_{n\ p}$, ns	7.8
$\tau_{p\ n}$, ns	$(10)_{CdS}$, $(1.33)_{ZnO}$, $(2.58)_{ZMO}$
$D_{n\ p}$, cm^2/s	25
$D_{n\ n}$, cm^2/s	$(5)_{CdS}$, $(7.5)_{ZnO}$, $(1)_{ZMO}$
$D_{p\ p}$, cm^2/s	2
T, K	300

In this part, nearly all carriers are collected, since the field rapidly drives them toward contacts.

The B contribution represents the losses in the diffusion region outside the SCR. Carriers generated there must reach the SCR boundary via diffusion. If the diffusion length is short, they recombine and do not contribute to the current.

The expression (A.1) does not account for recombination in the quasi-neutral regions of the window and absorbing layers, nor for recombination at the back surface. To include such losses, the diffusion component of the internal quantum yield ($Q_{dif\ p(n)}$) was calculated [45], and expressed as a product of three contributions (see Appendix 1, Eq. (A.2) for full expression):

$$Q_{dif\ p(n)} = A \times \left(B - \frac{C}{N}\right)$$

The factor A defines the extent to which photons, and the corresponding generation in the quasi-neutral region, can actually be collected through diffusion to the SCR boundary.

The factor B accounts for the contribution that could be collected from all generation in the neutral region under the assumption of no bulk or surface losses.

The factor C reflects losses at the back surface, bulk diffusion recombination in the quasi-neutral region, and generation within the absorbing layer volume.

The factor N serves as a normalization factor for the boundary conditions at the interface of the quasi-neutral region and the back surface.

The total internal quantum yield (Q_{int}) of the SC is defined as the sum of the drift and diffusion contributions, accounting for the directions of carrier transport. By additionally considering the optical losses due to reflection and absorption in the auxiliary layers (glass, ITO, CdS, ZnO, and ZMO), the external quantum yield (Q_{ext}) can be determined as:

$$Q_{ext} = T(\lambda) Q_{int}. \tag{17}$$

The short-circuit current density (J_{sc}) of the SC was calculated using the expression:

$$J_{sc} = q \sum_i T(\lambda) \frac{E_i(\lambda_i)}{h\nu_i} Q_{int}(\lambda_i) \Delta\lambda_i, \tag{18}$$

where, $E_i(\lambda_i)$ – solar spectral irradiance; $\Delta\lambda_i$ – the interval between adjacent wavelength values; $h\nu_i$ – the photon energy.

The calculation of J_{sc} was performed for illumination under the AM1.5G solar spectrum [36]. The maximum possible short-circuit current density ($J_{max\ sc}$) was estimated under ideal conditions, assuming no optical losses, $T(\lambda) = 1$, and full collection of photons, $Q_{ext}(\lambda) = 1$.

With known input power (P_{in}), the energy conversion efficiency (η) was determined [49]:

$$\eta = \frac{U_{oc} \cdot J_{sc} \cdot FF}{P_{in}}, \tag{19}$$

where, U_{oc} – open circuit voltage; J_{sc} – short circuit current density; FF – fill factor.

The fill factor (FF) was evaluated from the maximum power point parameters [49]:

Table 4
Calculated characteristics of the n-CdS(ZnO, ZMO)/p-CAS SCs.

Parameter	n-CdS/p-CAS	n-ZnO/p-CAS	n-ZMO/p-CAS
ΔE_c, eV	−1.43	−1.03	−0.03
ΔE_v, eV	2.15	2.73	2.33
V_D, eV	0.02	0.19	1.18
V_{CAS}, eV	0.01	0.11	0.61
V_{CdS}, eV	0.01	–	–
V_{ZnO}, eV	–	0.08	–
V_{ZMO}, eV	–	–	0.57

$$FF = \frac{I_m \cdot U_m}{I_{sc} \cdot U_{oc}}, \tag{20}$$

where, I_m, U_m – the current and voltage at the maximum power point.

During the calculation of recombination losses, the position of the Fermi level in the contacting materials was assumed to coincide with the energy levels associated with their dominant intrinsic point defects [15,17,18,44,47,48]. The resulting values of conduction band and valence band offsets (ΔE_c, ΔE_v), built-in potential (V_D), and potential drops across individual layers (V_{CAS}, V_{CdS}, V_{ZMO}, V_{ZnO}) are summarized in Table 4. Based on these parameters, idealized energy band diagrams of *n*-CdS(ZnO, ZMO)/*p*-CAS heterojunctions were constructed and are presented in Fig. 4. The analysis revealed that magnesium doping enhances conduction band alignment between ZMO and CAS, which contributes to an increased open-circuit voltage (U_{oc}).

3. Model Assumptions

It should be noted that Eq. (6) does not account for multiple internal reflections of light within the glass, ITO, CdS, ZnO, and ZMO layers. The reason is that, as shown in Ref. [41], interference effects in real multilayer structures (e.g., glass/ITO/CdS) are significantly

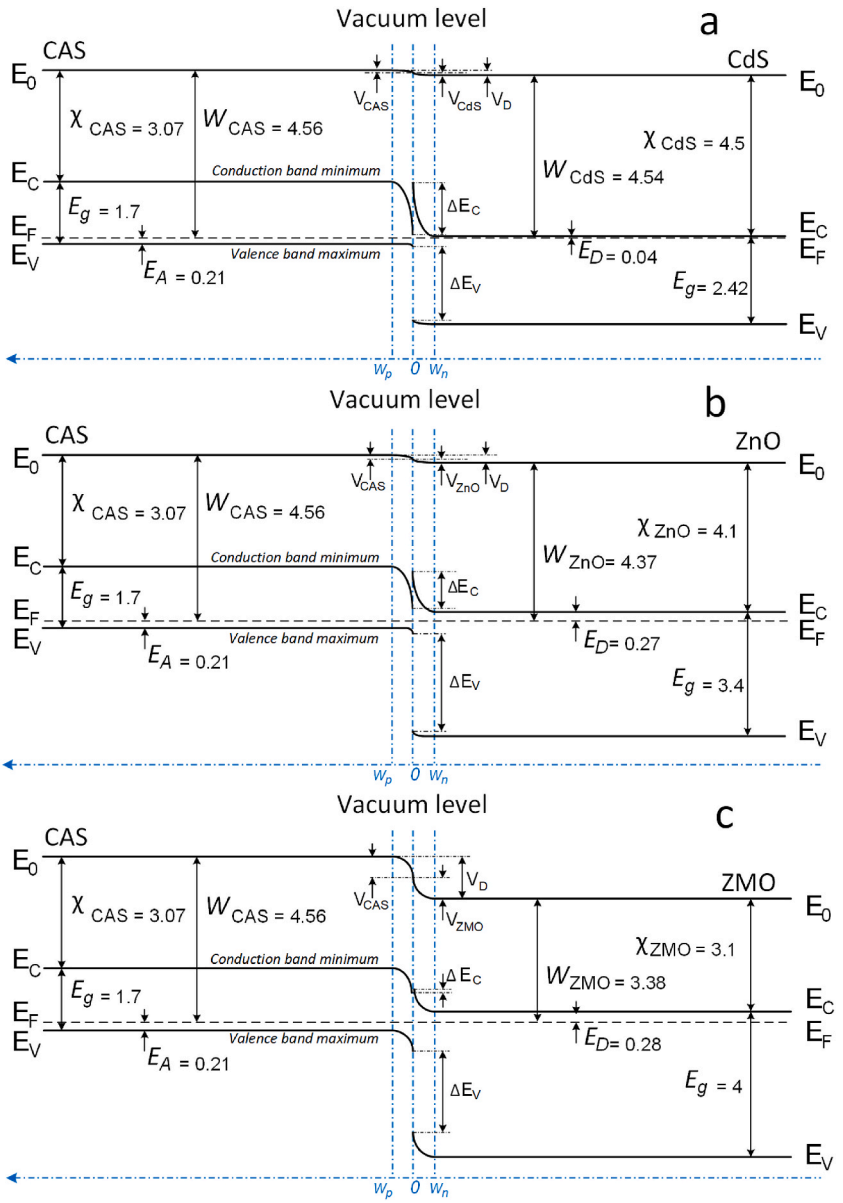

Fig. 4. Energy band diagram of (a) *n*-CdS/*p*-CAS, (b) *n*-ZnO/*p*-CAS, (c) *n*-ZMO/*p*-CAS.

weaker than in thin films in contact with air (the amplitude of transmission oscillations is 5–7 times smaller), since the refractive indices of adjacent layers are relatively close to each other, and the maxima and minima corresponding to layers of different thickness and refractive index n do not coincide. As a result, the interference maxima are smoothed out, and the average value of $T(\lambda)$ calculated without interference using Eq. (6) practically coincides (within 1–2 % accuracy) with that obtained from more precise formulas. Since the short-circuit current density J_{sc} is an integral quantity over the entire spectrum, the impact of weak oscillations on the result is negligible, and interference terms in $T(\lambda)$ formulas can be safely omitted without introducing significant errors.

When calculating recombination losses, the expression for the internal photoelectric quantum efficiency of a Schottky diode in a p-type semiconductor, derived from the continuity equation with surface recombination considered, is given as:

$$Q_{drift\ p(n)} = \frac{1 + \left(\frac{S}{D_p}\right)\exp\left(-\frac{W^2}{W_0^2}\right)[A(\alpha) - D_1(\alpha)]}{1 + \left(\frac{S}{D_p}\right)\exp\left(-\frac{W^2}{W_0^2}\right)B} - \frac{e^{(-\alpha W)}}{1 + \alpha L_n} - D_2(\alpha), \tag{21}$$

where,

$$W_0 = \left[\frac{2\varepsilon\varepsilon_0 kT}{q^2(N_a - N_d)}\right]^{1/2}, \tag{22}$$

$$A(\alpha) = \int_0^W exp\left[-\alpha x + \left(\frac{x - W}{W_0}\right)^2\right]dx, \tag{23}$$

$$B(\alpha) = \int_0^W exp\left(\frac{x - W}{W_0}\right)^2 dx, \tag{24}$$

where, α – absorption coefficient; $D_1(\alpha) = \left(D_n / D_p\right)F_5(\alpha)$; $D_2(\alpha) = \left(1 / L_p\right)F_5(\alpha)$, where $F_5(\alpha)$ – a quantity whose dependence on α is expressed through integrals (21) and (22); S – surface recombination velocity; D_n and D_p – electron and hole diffusion coefficients; L_n and L_p – electron and hole diffusion lengths.

However, for convenience in analyzing the dependence of η on the parameters of the diode structure, expression (21) can be simplified [46]. At the boundary between the SCR and the neutral region ($x = W$), photogenerated holes are swept into the SCR by the strong electric field, and it can be assumed that $\Delta p(\mathrm{W}) = 0$. This allows the terms $D_1(\alpha)$ and $D_2(\alpha)$ in (23) to be neglected without significant loss of accuracy. The integrand function $f(x)$ in expression (23) decreases exponentially with increasing x. Thus, the integration can be approximated by multiplying the maximum value of the function $f_{max}(0) = \exp(W/W_0)^2$ by its "half-width", defined as the value of x at the point where $f(x)$ falls to $1/e$ (≈2.71) of its maximum.

The value of x that satisfies this condition can be found from the equality:

$$e^{-\alpha x + \left(\frac{x-W}{W_0}\right)^2} = e^{\left(\frac{W}{W_0}\right)^2} e^{-1},$$

which reduces to a quadratic equation:

$$x^2 - \left(\alpha W_0^2 + 2W\right)x + W_0^2 = 0,$$

the solution of which is given by the following:

$$x = \frac{\alpha W_0^2 + 2W}{2}\left(1 - \sqrt{1 - \frac{4W_0^2}{\left(\alpha W_0^2 + 2W\right)^2}}\right) \approx \left(\alpha + \frac{2W}{W_0^2}\right)^{-1} = \left(\alpha + \frac{2}{w}\frac{\varphi_0 - qV}{kT}\right)^{-1},$$

(since the second term under the square root is much smaller than one, $\sqrt{1 - x} \approx 1 - x/2$).

Similarly, by replacing the integration in expression (24), the dependence for x can be obtained in the form:

$$x \approx \left(\frac{2}{w}\frac{\varphi_0 - qV}{kT}\right)^{-1},$$

Thus, the dependence of the internal quantum efficiency on α can be expressed as in (A.1).

Using a combination of parameters corresponding to the largest deviation between the Q_{ext} curves calculated from the exact (21) and simplified (A.1) expressions over a wide range of α, it can be observed that expression (A.1) approximates expression (21) very well even in this case (curve deviation <3.6 %). Moreover, surface recombination is most pronounced at low N_a–N_d and low electric field intensity, in the short-wavelength region (for N_a–$N_d = 10^{16}$–10^{17} cm^{-3}, this effect is practically negligible).

Within the applied model, we employ analytical expressions based on the continuity equation, accounting for key factors determining quantum efficiency, along with the Sah–Noyce–Shockley theory for generation–recombination in the SCR. However, this model does not consider recombination energy losses at interfacial defects of the ZMO/CAS boundary. We agree that selecting

materials with closely matched crystallographic parameters is crucial for forming an efficient heterojunction. In our case, the wurtzite phase of ZnMgO ($C_{Mg} = 0$) has lattice parameters $a = 0.31438$ nm and $c = 0.50367$ nm, while $Cu_{12}Sb_4S_{13}$ crystallizes in the cubic tetrahedrite structure with $a \approx 1.033$ nm. Analysis of the crystallographic compatibility between the ZMO window layer and the CAS absorbing layer shows that for the most energetically favorable epitaxial orientation ZMO(0001)/CAS(111). In this case, the minimum lattice mismatch is ~5 %. Such a value, in the case of direct contact, would lead to the generation of misfit dislocations at the heterointerface, acting as recombination centers and reducing the efficiency of the solar cell.

At the same time, the introduction of an isovalent Mg dopant into ZnO enables control over the physical properties of the solid solution $Zn_{1-x}Mg_xO$. By varying the magnesium concentration, one can adjust the lattice constant, the bandgap (from 3.3 eV for wurtzite ZnO to 7.8 eV for cubic MgO), and the electron work function, thereby optimizing the heterointerface and the conduction and valence band offsets (ΔE_c and ΔE_v).

An additional source of defects at the heterointerface may arise from the difference in thermal expansion coefficients (TEC) between ZMO ($\approx 6.5 \times 10^{-6}$ K^{-1}) and CAS.

($\approx 8.9 \times 10^{-6}$ K^{-1}). Thus, although the ZMO/CAS heterojunction exhibits excellent conduction band alignment, the efficiency values reported in this work reflect only the upper (theoretical) limit of possible performance. The impact of misfit dislocations can be further investigated through experimental characterization of actual devices, which is planned for future studies.

It should be noted that well-established methods exist to improve the quality of heterointerfaces. One of the most effective approaches is the introduction of thin buffer layers to compensate for lattice mismatch between contacting materials [55–57]. Another option is post-growth annealing of multilayer structures to form diffused intermediate layers [58–60].

4. Results and discussion

Fig. 5 shows the dependencies of the solar radiation absorptivity, both in terms of power (A_{sr}) and photon flux (A_{hv}), on the thickness of the CAS absorbing layer. It was found that 80 % of incident solar radiation is absorbed in a 500 nm-thick CAS layer, while at 2 μm this value increases to 90 %. As expected, at smaller thicknesses, the photon flux absorptivity (A_{hv}) is lower than the power absorptivity (A_{sr}). Notably, experimental studies have reported the highest efficiency values for photovoltaic devices with CAS absorbing layers in the (0.5–3.0) μm thickness range [13,61], which correlates well with these calculations. Beyond this thickness range, light absorption tends to saturate while the series resistance of the device increases, limiting further performance gains. An additional enhancement in A_{hv} can be achieved by reducing the absorbing layer thickness and increasing the absorption coefficient through doping with zinc or selenium, which can raise α to 10^5 cm^{-1} [9]. Further improvements in A_{sr} and A_{hv} are also possible through surface texturing, the use of anti-reflective coatings on the front side, and the rear ohmic contacts that reflect unabsorbed light. Moreover, nanostructuring can increase the effective area for photon interaction [62].

The calculated spectral dependencies of the reflection coefficient at the interfaces between SC layers and air are presented in Fig. 6. The analysis shows that the ZMO layer exhibits the lowest reflection in the spectral region $\lambda \leq 800$ nm ($R = 0.080$–0.155), demonstrating the beneficial effect of Mg doping, which layers are commonly used as reflective coatings for SC and other optoelectronic devices [63]. In the infrared region ($\lambda > 850$ nm), however, ITO maintains an advantage with lower reflection values ($R = 0.020$–0.071).

The reflection coefficient at the air/ITO interface increases sharply as the wavelength decreases, thus, in the ultraviolet region ($\lambda \leq 360$ nm), ZnO performs better. For the air/CAS and air/glass interfaces, the reflection coefficients fall within the ranges of 0.070–0.210 and 0.035–0.040, respectively. The spectral dependencies of the reflection coefficients at the interfaces between adjacent layers in the solar cell structure are shown in Fig. 7. As seen in Fig. 7a, the reflection at the glass/ITO interface decreases monotonically for

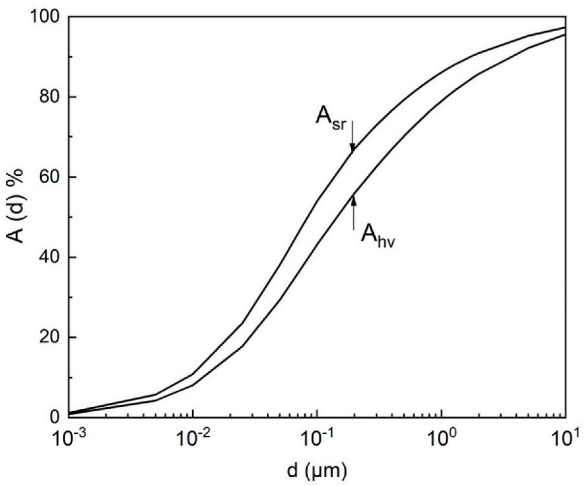

Fig. 5. Absorptivity of solar radiation (A_{sr}) and photon flux (A_{hv}) depending on the thickness of the CAS layer.

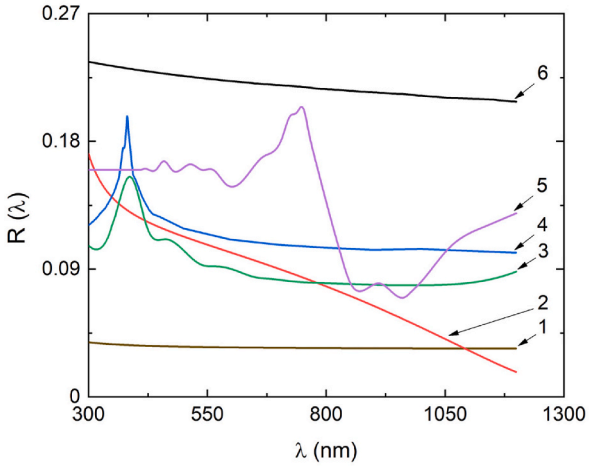

Fig. 6. Spectral dependencies of reflection coefficients (R) for the following interfaces: air/glass (1), air/ITO (2), air/ZMO (3), air/ZnO (4), air/CAS (5), air/CdS (6).

wavelengths below $\lambda = 1100$ nm, and then slightly increases. Fig. 7b illustrates that the reflection at the ITO/ZnO interface becomes comparable to that at the ITO/ZMO interface only within a specific spectral range ($\lambda = 400$–700 nm), beyond which the ITO/ZMO configuration exhibits superior performance. Notably, at $\lambda \approx 1200$ nm, the reflection coefficient for the ITO/ZMO interface ($R = 0.027$) is approximately 36 % lower than that for the ITO/ZnO interface ($R = 0.042$). The ITO/CdS interface demonstrates inferior performance, with reflection coefficients ranging from $R = 0.020$ to 0.080 across the entire spectral range.

In general, the R values at internal interfaces between functional layers are relatively low, which is attributed to the small

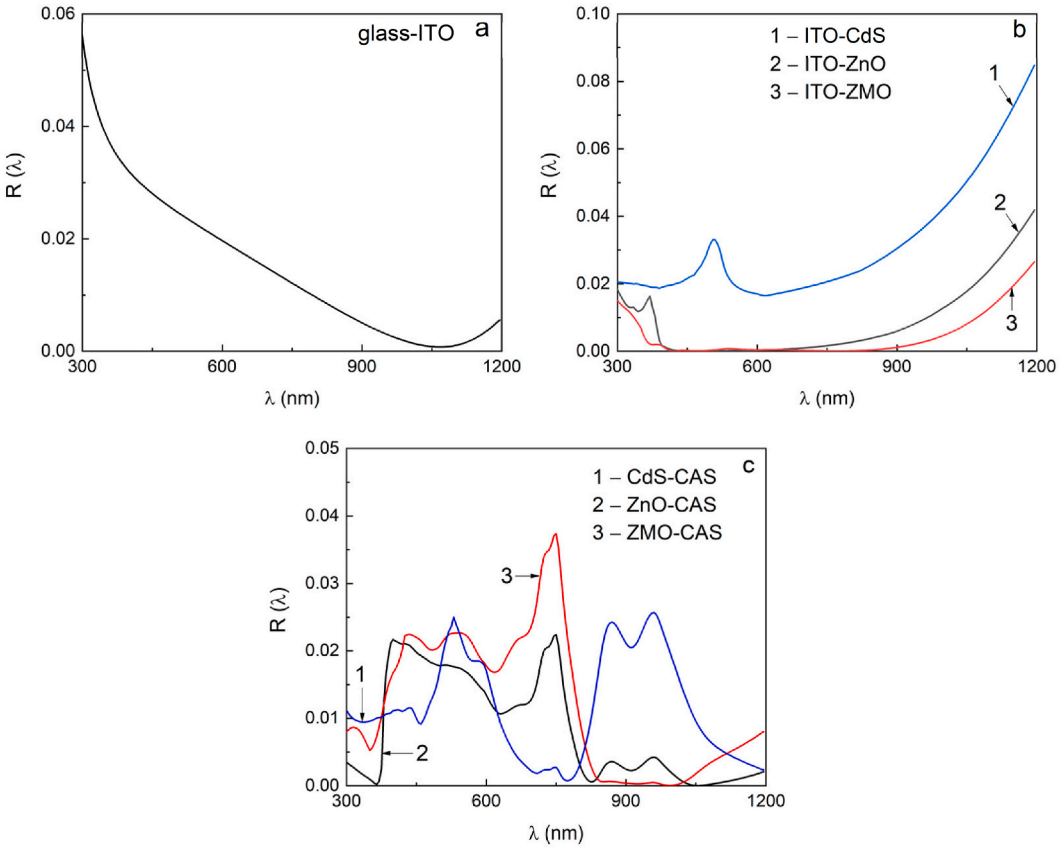

Fig. 7. Spectral dependencies of the reflection coefficients (R) at the interfaces between contacting layers in the solar cell structure: (a) glass/ITO, (b) ITO/window, (c) window/CAS.

differences in their optical constants. In contrast, interfaces between these same materials and air exhibit significantly higher reflection coefficients. Fig. 7c presents the calculated reflection coefficients at the heterointerfaces between the CAS absorbing layer and the window layers (CdS, ZnO, ZMO).

The results indicate that these interfaces yield low reflection values ($R < 0.040$), suggesting that they are well-suited for use in photovoltaic devices requiring minimal optical reflection losses. Among them, ZnO provides the lowest reflection at the window/absorbing layer interface, with values below $R = 0.021$ and an average of $R = 0.008$ across the investigated spectral range, compared to $R = 0.012$ for CdS.

The corresponding spectral dependencies of the light transmission coefficients for SC with *n*-CdS(ZnO, ZMO)/*p*-CAS heterojunctions and ITO front contact are shown in Fig. 8. The optical loss coefficients (Δ), expressed as percentages, for each of the evaluated structures are summarized in Table 5. The table also includes the corresponding light penetration coefficients into the absorbing layer. The lowest optical losses were observed for the SC with the ITO/ZMO/CAS (Δ = 6.50 %, $T = 93.50$ %), while the highest losses were recorded for the ITO/CdS/CAS (Δ = 9.07 %, $T = 90.93$ %). This indicates that even combinations of conductive (ITO) and window (CdS) layers can still provide relatively high light transmittance to the CAS absorbing layer. It is noteworthy that the difference in optical losses between the best and worst-performing SCs does not exceed 2.60 %. This suggests that further optimization of the SCs should focus on other factors, such as absorption losses within the auxiliary layers, carrier recombination, and the crystalline quality of the materials.

Fig. 9 presents the spectral dependencies of the transmission coefficients for SCs considering photon absorption in the auxiliary layers. The simulations were carried out for current-collecting layer thicknesses d_{ITO} = 100–200 nm (Fig. 9a) and window layer thicknesses $d_{CdS(ZnO,ZMO)}$ = 25–100 nm (Fig. 9b), which are typical for practical SCs. The light loss coefficients are summarized in Table 6.

According to the results, minimizing the thicknesses of the auxiliary layers, within technological limits, is beneficial for reducing optical losses. Moreover, replacing the conventional CdS window layer with materials of wider bandgap, such as ZnO or ZMO, leads to improved transmittance of the multilayer structure. ZnO proves to be the most favorable window material, as it offers superior light transmission to the CAS absorbing layer compared to both ZMO and CdS. However, the overall gain from substituting CdS with ZnO or ZMO remains modest, not exceeding 2.31–2.70 %. Moreover, analysis of the results presented in Fig. 9 and Table 6 indicates that, among the investigated auxiliary layer thicknesses, the most favorable solar cell structure is *n*-ITO/*n*-ZnO/*p*-CAS.

Fig. 10 shows the calculated internal quantum yield (Q_{int}) as a function of wavelength for SC incorporating different concentrations of uncompensated acceptors (N_A) in the absorbing and donors (N_D) in the window layers. The simulations were conducted for SCs with a CAS absorbing layer thickness of 500 nm ($A_{hv} \approx 80$ %) and a window layer thickness of 25 nm.

The results indicate that increasing the donor concentration in the window layer, while keeping N_A constant in the absorbing layer, leads to an enhanced Q_{int} in the photosensitivity region of the respective window materials (CdS, ZnO, ZMO) (Fig. 10a–c, e). This enhancement is particularly evident in the short- and medium-wavelength regions and is attributed to the expansion of the space charge region within the absorbing layer, which reduces the influence of the diffusion component on the total photocurrent (J_{ph}). Further simulations were carried out to assess the impact of varying N_A in the CAS layer, with a fixed donor concentration in the window material (Fig. 10b–d, f).

The decrease in the acceptor concentration in the CAS absorbing layer leads to a reduction in the Q_{int} within the part ($\lambda < 730$ nm) of spectral range corresponding to the photosensitivity of the absorbing layer material.

However, further increases in acceptor concentration result in a decreased quantum yield. This behavior is attributed to the narrowing of the space charge region, which in turn increases the contribution of the diffusion part to the total J_{ph}. When evaluating the overall efficiency of the solar cell, it is essential to also account for optical losses in the auxiliary layers, as discussed in the previous

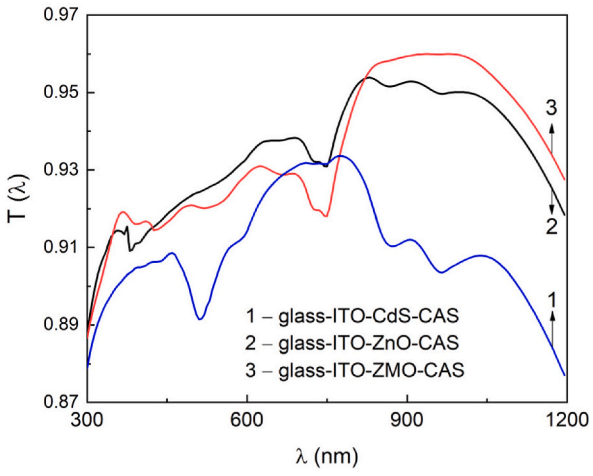

Fig. 8. Spectral dependencies of the transmission coefficients (*T*) for SC with the structure glass/ITO/window/CAS, considering light reflection at the interfacial boundaries.

Table 5
Values of loss coefficient (Δ) and light penetration for ITO/window/CAS SC.

No.	Solar cell	Optical loss coefficient, Δ (%)	Light penetration coefficient, %
1	ITO/CdS/CAS	9.07	90.93
2	ITO/ZnO/CAS	6.82	93.18
3	ITO/ZMO/CAS	6.50	93.50

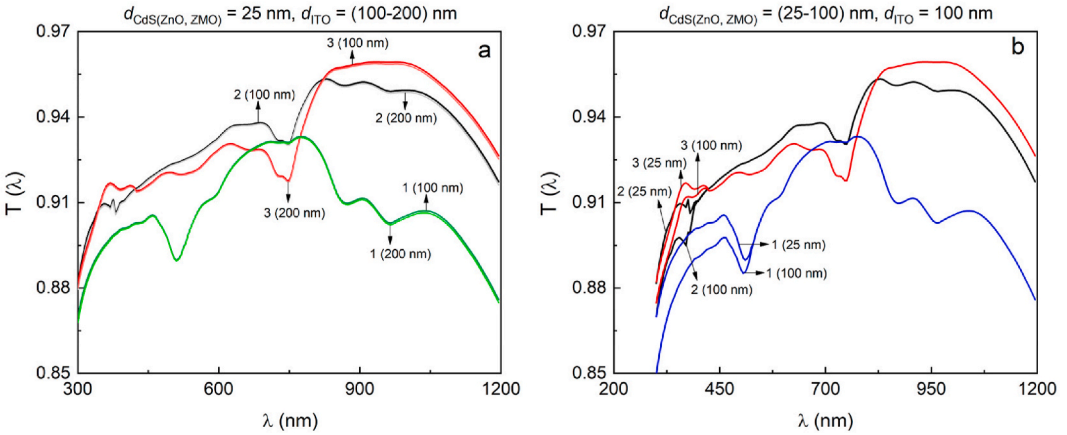

Fig. 9. Spectral dependencies of the transmission coefficients for SC with the structures glass/ITO/CdS/CAS (1), glass/ITO/ZnO/CAS (2), and glass/ITO/ZMO/CAS (3) at various thicknesses of the current-collecting and window layers. Both interfacial reflection and absorption in auxiliary layers are considered.

Table 6
Values of the light loss coefficient for SC with various structures (considering photon absorption in the auxiliary layers).

№	Solar cell	Loss coefficient, Δ (%)			
d_{ITO} = 100 nm					
$d_{CdS(ZnO, ZMO)}$, nm		25	50	75	100
1	ITO/CdS/CAS	9.22	9.30	9.39	9.48
2	ITO/ZnO/CAS	6.67	6.70	6.74	6.78
3	ITO/ZMO/CAS	7.10	7.12	7.15	7.17
d_{ITO} = 200 nm					
1	ITO/CdS/CAS	9.27	9.36	9.45	9.54
2	ITO/ZnO/CAS	6.73	6.77	6.80	6.84
3	ITO/ZMO/CAS	7.16	7.18	7.21	7.23

section. Taking these losses into consideration, the spectral dependence of Q_{ext} was calculated for the studied SC.

The calculations were carried out using the following material parameters: $N_A = 10^{14}$–10^{17} cm^{-3}, $N_D = 10^{15}$–10^{17} cm^{-3}, $d_{ITO} = 100$ nm, $d_{CdS,ZnO,ZMO} = 25$ nm, and $d_{CAS} = 0.5$ μm. The corresponding results are shown in Fig. 11.

Analysis of the obtained dependencies reveals that, despite ZnO having a slight advantage in light transmission (~0.4 %), the SC with the *n*-ZMO/*p*-CAS structure exhibits the highest Q_{ext}, particularly at $N_A = 10^{17}$ cm^{-3} and $N_D = 10^{18}$ cm^{-3}, which is attributed to changes in its electronic structure. In general, both doped and undoped ZnO window layers demonstrate superior Q_{ext} compared to traditional CdS layers. As expected, SC with window layers made of wider bandgap materials exhibit higher quantum yields. Specifically, the external quantum yield of ZnO increases more rapidly in the spectral range of 380–420 nm, while ZMO shows consistently higher Q_{ext} values (by 5–12 %) at longer wavelengths. The theoretical maximum short-circuit current density of the considered SC is $J_{max\ sc} = 27.04$ mA/cm^2. Practically, this value is unattainable due to inevitable losses during photovoltaic conversion. The calculations of short-circuit current density were carried out at $N_A = 10^{14}$ cm^{-3}, $N_D = 10^{17}$ cm^{-3}. These concentrations of uncompensated acceptors and donors result in SCR widths comparable to the thickness of the heterojunction. Additionally, calculations were carried out for concentrations demonstrating high Q_{ext} efficiency, $N_A = 10^{16}$ cm^{-3}, $N_D = 10^{17}$ cm^{-3}.

Fig. 12 illustrates the dependence of J_{sc} on the window layer thickness for SC with ITO/CdS(ZnO, ZMO)/CAS at different concentration values of $N_A = 10^{14}$–10^{16} cm^{-3}, $N_D = 10^{17}$ cm^{-3}, considering ITO thicknesses of 100 nm and 200 nm. Analysis shows that, at an acceptor concentration of 10^{16} cm^{-3}, higher short-circuit current density values (by 1.11–2.60 mA/cm^2) are observed. Under such conditions, with reflection and absorption losses in auxiliary layers included devices with the ITO/ZMO/CAS structure ($d_{ZnO} = 25$–100 nm, $d_{ITO} = 100$ nm) exhibit J_{sc} values higher by approximately 0.90–0.91 mA/cm^2 than those of ITO/ZnO/CAS devices across the full thickness range.

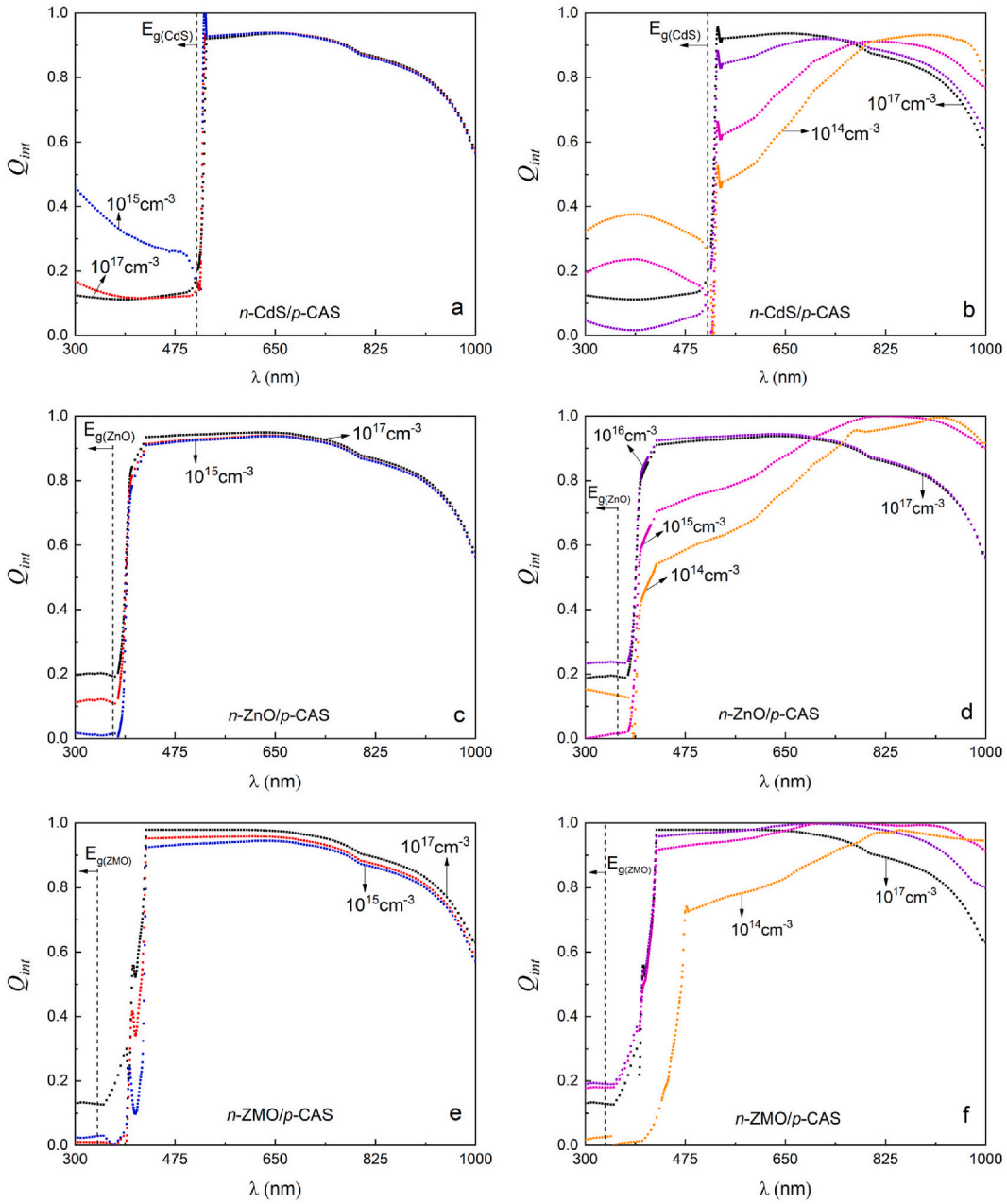

Fig. 10. Spectral dependency of the internal quantum yield (Q_{int}) of SC with (a, b) *n*-CdS/*p*-CAS, (c, d) *n*-ZnO/*p*-CAS, (e, f) *n*-ZMO/*p*-CAS heterojunctions at different concentration values of $N_A = 10^{14}$–10^{17} cm^{-3} and $N_D = 10^{15}$–10^{17} cm^{-3}.

It was found that increasing the thickness of the ITO layer to 200 nm leads to a decrease in the J_{sc}. The difference in J_{sc} between SC with ITO/ZMO/CAS and ITO/CdS/CAS structures ranges from 4.8 to 5.5 mA/cm^2. Notably, optical and recombination losses cause a reduction in J_{sc} by 23–41 % at $N_A = 10^{14}$ cm^{-3}, $N_D = 10^{17}$ cm^{-3}. However, at $N_A = 10^{16}$ cm^{-3} these losses exert less influence on the J_{sc}, reducing it by 20–37 %. To assess the impact of losses on the theoretical efficiency (η) of the ITO/CdS(ZnO, ZMO)/CAS, open-circuit voltage (U_{oc}) values were assumed to equal the contact potential difference at the heterojunctions: $U_{oc} = 0.02$ V for CdS, 0.13 V for ZnO, and 0.98 V for ZMO. Corresponding fill factor (*FF*) values were *FF* = 26 % for CdS, 67 % for ZnO, and 88 % for ZMO. Based on these parameters, the theoretical η of solar cell with ZMO window layer was found to be 23.75 %. At the same time, potential misfit dislocations or interfacial defects may lead to a reduction in efficiency (see Section 3, Model Assumptions).

The short-circuit current values achieved in experimental structures with similar architectures (e.g., $CuSbS_2$, CZTS) and the highest certified efficiencies were: 21.7 mA/cm^2 for CZTS with 11.0 % efficiency [64], 35.7 mA/cm^2 for CZTSSe with 13.8 % efficiency [7], and 26.0 mA/cm^2 for $CuSbS_2$ with 4.7 % efficiency [65].

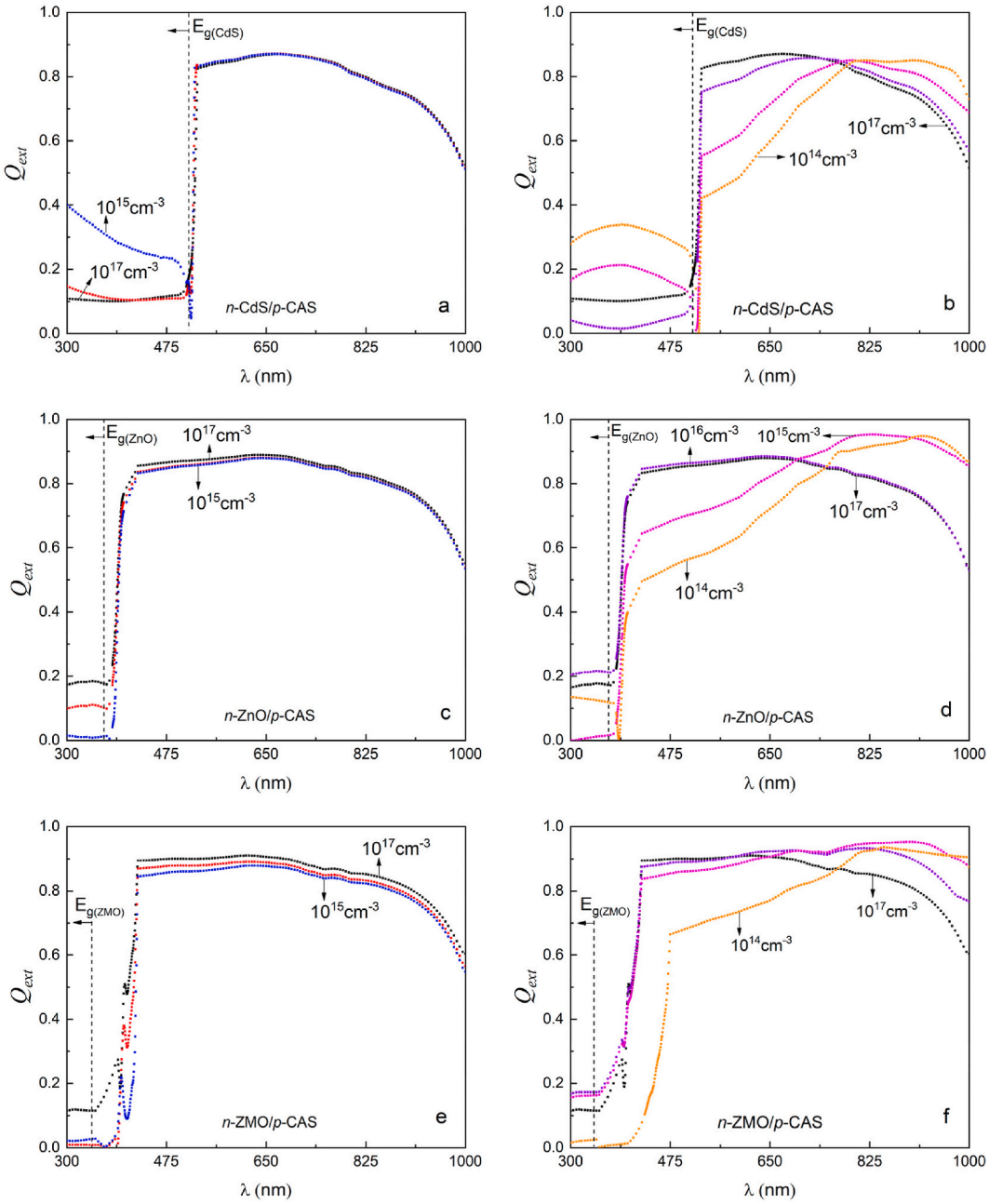

Fig. 11. Spectral dependency of the external quantum yield (Q_{ext}) of the SC with *n*-CdS(ZnO, ZMO)/*p*-CAS heterojunctions and ITO current-collecting layer at $N_A = 10^{14}$–10^{17} cm^{-3}, $N_D = 10^{15}$–10^{17} cm^{-3}, $d_{ITO} = 100$ nm, $d_{CdS(ZnO,ZMO)} = 25$ nm, and $d_{CAS} = 0.5$ μm.

Table 7 presents the dependence of efficiency (η) on the thickness of the window layers (CdS, ZnO, ZMO) and carrier concentration. Variation in the thickness of the current-collecting ITO layer has little effect on the overall efficiency. It is shown that efficiency values differ by 7–10 % depending on the carrier concentration, with higher values observed at $N_A = 10^{16}$ cm^{-3}, $N_D = 10^{17}$ cm^{-3}. The most efficient solar cell has the ITO/ZMO/CAS SC, achieving $\eta \approx 19.89$ % at $d_{ITO} = 100$ nm and $d_{ZMO} = 25$–100 nm, due to the high U_{oc}.

The authors of one experimental study, which reported a low SC efficiency [61], used undoped pure tetrahedrite with high carrier (hole) density. In this case, the material exhibited degenerate semiconductor behavior, with a side effect of high sample absorption (10^4 cm^{-1}), and, as the authors themselves noted very poor V_{oc} probably originated from the severe recombination or inappropriate band alignment, resulting in extremely low heterojunction voltage and poor conversion efficiency.

Doping with magnesium allows widening of the ZnO bandgap by raising the conduction band level. As a result, the higher energy barrier for holes improves selectivity for electrons, suppressing their backflow. The main factor enhancing the external quantum

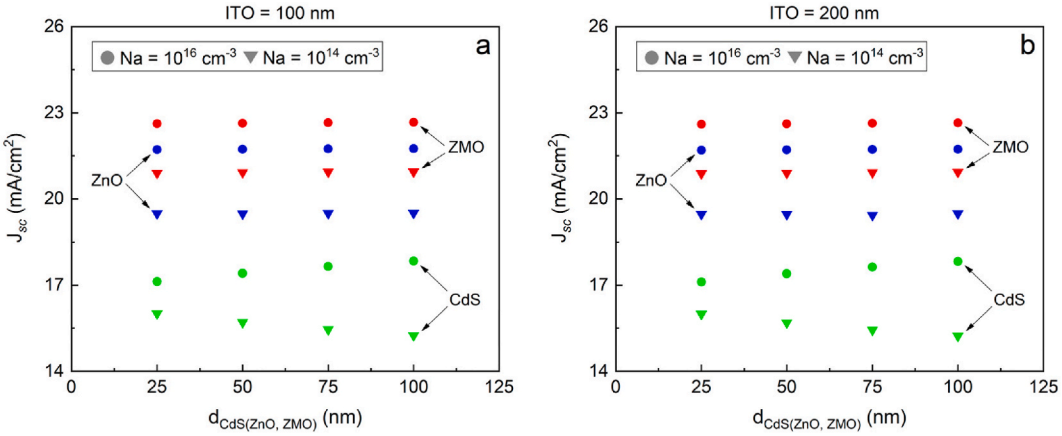

Fig. 12. Dependence of the short-circuit current density (J_{sc}) on the thickness of the window layer for SC with CdS/CAS, ZnO/CAS, ZMO/CAS heterojunctions, with the thickness of the current-collecting layer (ITO): (a) 100 nm and (b) 200 nm.

Table 7
Efficiency η (%) of SC with ITO/CdS(ZnO, ZMO)/CAS heterojunctions.

N°	Solar cell	Window layer thickness, nm			
$N_A = 10^{14}$ cm^{-3}, $N_D = 10^{17}$ cm^{-3}, $d_{ITO} = 100$ nm					
$d_{CdS(ZnO,ZMO)}$, nm		25	50	75	100
1	ITO/CdS/CAS	0.29	0.29	0.28	0.28
2	ITO/ZnO/CAS	0.91	0.91	0.91	0.91
3	ITO/ZMO/CAS	17.88	17.9	17.91	17.92
$N_A = 10^{14}$ cm^{-3}, $N_D = 10^{17}$ cm^{-3}, $d_{ITO} = 200$ nm					
1	ITO/CdS/CAS	0.29	0.29	0.28	0.28
2	ITO/ZnO/CAS	0.91	0.91	0.91	0.91
3	ITO/ZMO/CAS	17.87	17.88	17.9	17.91
$N_A = 10^{16}$ cm^{-3}, $N_D = 10^{17}$ cm^{-3}, $d_{ITO} = 100$ nm					
1	ITO/CdS/CAS	0.31	0.32	0.32	0.32
2	ITO/ZnO/CAS	1.89	1.89	1.89	1.89
3	ITO/ZMO/CAS	19.87	19.88	19.90	19.91
$N_A = 10^{16}$ cm^{-3}, $N_D = 10^{17}$ cm^{-3}, $d_{ITO} = 200$ nm					
1	ITO/CdS/CAS	0.31	0.32	0.32	0.32
2	ITO/ZnO/CAS	1.89	1.89	1.89	1.89
3	ITO/ZMO/CAS	19.85	19.87	19.88	19.89

efficiency becomes a more effective diffusion component of carriers collected from the absorbing layer volume and transported to the heterojunction. This reduces bulk SRH losses and carrier recombination, thereby enabling higher open-circuit voltage and overall device efficiency.

For comparison, the typical ITO/CdS/CAS design exhibits an $\eta \approx 0.32$ %, consistent with reported experimental values for tetrahedrite-based SC ($\eta \approx 0.04$–0.14 %) [21,61]. The SC with a ZnO window layer show efficiencies around $\eta \approx 1.89$ %. Fig. 13 shows

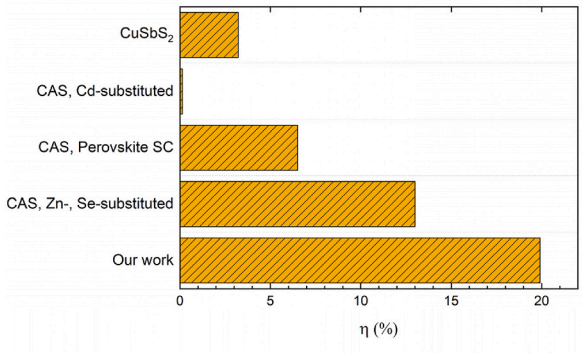

Fig. 13. Our simulated η vs literature-reported values for CAS SCs.

a comparison of calculated efficiency (η) values with literature data for SCs using tetrahedrite: 13 % for CAS doped with Zn and Se [9]; 6.5 % for perovskite SCs with CAS as a hole transport layer [12]; 0.14 % for CAS doped with Cd [21]; and 3.22 % for $CuSbS_2$ [66].

5. Conclusion

Optical and recombination losses in SCs with *n*-CdS(ZnO, ZnMgO)/*p*-CAS heterojunctions were found to reduce J_{sc} by 23–41 % at $N_A = 10^{14}$ cm^{-3} and by 20–37 % at $N_A = 10^{16}$ cm^{-3}. Notably, the absorptivity of solar radiation (A_{sr}) reaches 80 % at a CAS absorbing layer thickness of only 500 nm, increasing to over 90 % for $d_{CAS} \approx 2$ μm. Wider-bandgap windows (ZnO, ZMO) enhance short-wavelength transmission compared to CdS, with ZnO exhibiting superior spectral transparency ($T = 93.5$ %).

Spectral analysis of Q_{ext} revealed that *n*-ZMO/*p*-CAS heterojunction devices exhibit higher external quantum yields, particularly at $N_A = 10^{16}$ cm^{-3} and $N_D = 10^{17}$ cm^{-3}. The highest J_{sc} (22.67 mA/cm^2) and efficiency ($\eta = 19.91$ %) was obtained for the ITO/ZMO/CAS configuration at $d_{ZMO} = 100$ nm and $N_A = 10^{16}$ cm^{-3}, $N_D = 10^{17}$ cm^{-3}. The J_{sc} difference compared to the ITO/CdS/CAS structure was 4.8–5.5 mA/cm^2 at $d_{CdS(ZnO)} = 25$–100 nm. Doping ZnO with Mg enhanced the conduction band alignment between the window material and *p*-CAS, leading to increased open-circuit voltage and overall solar cell efficiency. Employing undoped *n*-ZnO resulted in $\eta = 1.89$ %, while the conventional ITO/CdS/CAS design showed only 0.32 %.

Nanocrystalline CAS and the corresponding films have already been produced for practical applications [14,67,68]. The modeling results presented above provide a foundation for optimizing light absorption and charge carrier collection processes and enable the formulation of recommendations for the development of high-efficiency CAS-based SCs.

1. Doping of CAS with 2+ transition metals, such as Zn or Mn, is required to convert it into a non-degenerate semiconductor with a charge carrier concentration of ~10^{16} cm^{-3}.
2. The use of new window materials with an optimal energy structure is necessary. A prime example is the *n*-ZnMgO solid solution, which combines a wide bandgap with an electron affinity close to that of tetrahedrite. The optimal charge carrier concentration in the window material is 10^{17} cm^{-3}.
3. It has been found that a CAS film absorbs ~80 % of solar radiation at a thickness of only ~500 nm, allowing the use of ultra-thin absorbing layers of this material. As a result, significant material savings are achieved, leading to a corresponding reduction in the fabrication cost of photovoltaic devices. However, CAS requires doping to reach a non-degenerate state. Ideally, this dopant level should result in a SCR thickness equal to that of the absorbing layer, so that the built-in electric field effectively facilitates the separation of photogenerated charge carriers, thereby enhancing the SC efficiency.
4. Doped tetrahedrite has a bandgap of $E_g = 1.7$ eV, which is also optimal for use of this material in multi-junction thin-film tandem SC.

6. Future work

The experimental implementation of the proposed strategies to enhance the efficiency of CAS-based SCs includes.

1. Preparing non-degenerate CAS films using low-cost chemical methods by doping the material with Zn, Ni, Sn, or Se. Tetrahedrite nanoparticles are expected to be synthesized using a colloidal–polyol method. This approach enables the formation of nanosized particles with tailored structural, optical, electrical, and consequently functional properties. For film deposition, low-energy, chemically based, and resource-efficient techniques such as spin coating, spray pyrolysis, or inkjet printing are proposed. These methods have proven effective for producing uniform tetrahedrite thin films, providing control over film thickness, coating uniformity, and process scalability. In the case of ZnMgO, the films are planned to be deposited using spray pyrolysis.
2. Measuring optoelectronic and thermoelectric properties to optimize the charge carrier concentration and bandgap width.
3. Selecting the window material to achieve optimal lattice matching with the contacting materials and proper energy alignment in their band diagram.
4. Fabricating multilayer structures containing the heterojunction and auxiliary layers, including current-collecting contacts, with post-growth annealing optimized to improve interfacial quality.

CRediT authorship contribution statement

Artem Zabuha: Writing – original draft, Visualization, Investigation. **Oleksandr Dobrozhan:** Writing – review & editing, Investigation, Funding acquisition, Conceptualization. **Dmytro Velykodnyi:** Investigation. **Anatoliy Opanasyuk:** Writing – review & editing, Supervision, Conceptualization.

Declaration of competing interest

The authors declare that they have no known competing financial interests or personal relationships that could have appeared to influence the work reported in this paper.

Acknowledgments

This work was supported by the Ministry of Education and Science of Ukraine (0124U000541).

Appendix 1. Detailed expressions for the drift and diffusion components of the internal quantum efficiency

The drift component of the internal quantum efficiency (Q_{drift}):

$$Q_{drift\ p(n)} = \frac{1 + \frac{S}{D_{p\ \rho(n\ n)}}\left(\alpha_{p(n)} + \frac{2\cdot(V_D - qU)}{w_{p(n)}\cdot k_B T}\right)^{-1}}{1 + \frac{S}{D_{p\ \rho(n\ n)}}\left(\frac{2\cdot(V_D - qU)}{w_{p(n)}\cdot k_B T}\right)^{-1}} - \frac{e^{-\alpha_{p(n)} w_{p(n)}}}{1 + \alpha_{p(n)}\cdot L_{n\ p(p\ n)}}, \tag{A.1}$$

$$Q_{drift\ p(n)} = A - B,$$

$$A = \frac{1 + \frac{S}{D_{p\ \rho(n\ n)}}\left(\alpha_{p(n)} + \frac{2\cdot(V_D - qU)}{w_{p(n)}\cdot k_B T}\right)^{-1}}{1 + \frac{S}{D_{p\ \rho(n\ n)}}\left(\frac{2\cdot(V_D - qU)}{w_{p(n)}\cdot k_B T}\right)^{-1}},$$

where, S – the recombination rate of carriers at the boundary of the heterojunction and in the SCR; $D_{\text{p p(n n)}}$ – the diffusion coefficients of holes and electrons in the absorbing and window layers; $\alpha_{\text{p(n)}}$ – the light absorption coefficient in the absorbing and window layers; k_{B} – the Boltzmann constant; T – the temperature.

The A contribution describes the collection of carriers generated within the depletion region, where a strong electric field is present. In this part, nearly all carriers are collected, since the field rapidly drives them toward contacts.

$$B = \frac{e^{-\alpha_{p(n)} w_{p(n)}}}{1 + \alpha_{p(n)}\cdot L_{n\ p(p\ n)}},$$

where, $L_{\text{n p(p n)}}$ – the diffusion length of electrons and holes in the absorbing and window layers; $L_{n(p)} = \left(\tau_{n(p)}\cdot D_{n(p)}\right)^{1/2}$, where $\tau_{\text{n(p)}}$ – the lifetime of electrons and holes, $D_{\text{n(p)}}$ – the diffusion coefficients of electrons and holes in the corresponding layers.

The B contribution represents the losses in the diffusion region outside the SCR. Carriers generated there must reach the SCR boundary via diffusion. If the diffusion length $L_{n(p)}$ is short, they recombine and do not contribute to the current.

The diffusion component of the internal quantum yield ($Q_{\text{dif p(n)}}$):

$$Q_{dif\ p(n)} = \left(\alpha_{p(n)} L_{n\ p(p\ n)} \Big/ \left(\alpha_{p(n)}{}^2 L^2_{n\ p(p\ n)} - 1\right)\right) e^{-\alpha_{p(n)} w_{p(n)}} \times \left(\alpha_{p(n)} L_{n\ p(p\ n)} - \left(\frac{\left(S_b L_{n\ p(p\ n)} / D_{n\ p(p\ n)}\right)\left(cosh\ E - e^{\left(-\alpha_{p(n)}\left(d_{p(n)} - w_{p(n)}\right)\right)}\right) + sinh\ E + \alpha_{p(n)} L_{n\ p(p\ n)} e^{\left(-\alpha_{p(n)}\left(d_{p(n)} - w_{p(n)}\right)\right)}}{\left(S_b L_{n\ p(p\ n)} / D_{n\ p(p\ n)}\right) sinh\ E + cosh\ E}\right)\right), \tag{A.2}$$

$$Q_{dif\ p(n)} = A \times \left(B - \frac{C}{N}\right)$$

$$A = \left(\alpha_{p(n)} L_{n\ p(p\ n)} \Big/ \left(\alpha_{p(n)}{}^2 L^2_{n\ p(p\ n)} - 1\right)\right) e^{-\alpha_{p(n)} w_{p(n)}},$$

The factor A defines the extent to which photons, and the corresponding generation in the quasi-neutral region, can actually be collected through diffusion to the SCR boundary.

$$B = \alpha_{p(n)} L_{n\ p(p\ n)}.$$

The factor B accounts for the contribution that could be collected from all generation in the neutral region under the assumption of no bulk or surface losses.

$$C = \left(S_b L_{n\ p(p\ n)} / D_{n\ p(p\ n)}\right)\left(cosh\ E - e^{\left(-\alpha_{p(n)}\left(d_{p(n)} - w_{p(n)}\right)\right)}\right) + sinh\ E + \alpha_{p(n)} L_{n\ p(p\ n)} e^{\left(-\alpha_{p(n)}\left(d_{p(n)} - w_{p(n)}\right)\right)}$$

where, S_{b} –recombination velocity on the back of absorbing layer and front of window layers, $E = \left(d_{p(n)} - w_{p(n)}\right)/L_{n\ p(p\ n)}$, $d_{\text{p(n)}}$ – thickness of absorbing or window layers.

The factor C reflects losses at the back surface, bulk diffusion recombination in the quasi-neutral region, and generation within the absorbing layer volume.

$$N = \left(S_b L_{n\,p(p\,n)} \,/\, D_{n\,p(p\,n)}\right) sinh\, E + cosh\, E$$

The factor N serves as a normalization factor for the boundary conditions at the interface of the quasi-neutral region and the back surface.

Data availability

Data will be made available on request.

References

[1] G. Wang, Z. Zhang, J. Lin, Multi-energy complementary power systems based on solar energy: a review, Renew. Sustain. Energy Rev. 199 (2024) 114464, https://doi.org/10.1016/j.rser.2024.114464.

[2] D.N. Madsen, J.P. Hansen, Outlook of solar energy in Europe based on economic growth characteristics, Renew. Sustain. Energy Rev. 114 (2019) 109306, https://doi.org/10.1016/j.rser.2019.109306.

[3] M. Green, E. Dunlop, M. Yoshita, N. Kopidakis, K. Bothe, G. Siefer, D. Hinken, M. Rauer, J. Hohl-Ebinger, X. Hao, Solar cell efficiency tables (Version 64), Prog. Photovolt. 32 (2024) 425–441, https://doi.org/10.1002/pip.3831.

[4] E.T. Efaz, M.M. Rhaman, S. Al Imam, K.L. Bashar, F. Kabir, S.N. Sakib, M.D.E. Mourtaza, A review of major technologies of thin-film solar cells, Eng. Res. Express 3 (2021) 032001, https://doi.org/10.1088/2631-8695/ac2353.

[5] J. Yi, G. Zhang, H. Yu, H. Yan, Advantages, challenges and molecular design of different material types used in organic solar cells, Nat. Rev. Mater. 9 (2023) 46–62, https://doi.org/10.1038/s41578-023-00618-1.

[6] I. Massiot, A. Cattoni, S. Collin, Progress and prospects for ultrathin solar cells, Nat. Energy 5 (2020) 959–972, https://doi.org/10.1038/s41560-020-00714-4.

[7] J. Zhou, X. Xu, H. Wu, J. Wang, L. Lou, K. Yin, Y. Gong, J. Shi, Y. Luo, D. Li, H. Xin, Q. Meng, Control of the phase evolution of kesterite by tuning of the selenium partial pressure for solar cells with 13.8% certified efficiency, Nat. Energy 8 (2023) 526–535, https://doi.org/10.1038/s41560-023-01251-6.

[8] A. Wang, M. He, Martin A. Green, K. Sun, X. Hao, A critical review on the progress of kesterite solar cells: current strategies and insights, Adv. Energy Mater. 13 (2022) 2203046, https://doi.org/10.1002/aenm.202203046.

[9] J. Heo, R. Ravichandran, Christopher F. Reidy, J. Tate, J. Wager, D. Keszler, Design meets nature: tetrahedrite solar absorbers, Adv. Energy Mater. 5 (2014) 1401506, https://doi.org/10.1002/aenm.201401506.

[10] A. Pfitzner, M. Evain, V. Petricek, $Cu_{12}Sb_4S_{13}$: a temperature-dependent structure investigation, Acta Crystallogr. B 53 (1997) 337–345, https://doi.org/10.1107/S0108768196014024.

[11] D. Weller, D. Morelli, Tetrahedrite thermoelectrics: from fundamental science to facile synthesis, Front. Electron. Mater. 2 (2022), https://doi.org/10.3389/femat.2022.913280.

[12] M. Tamilselvan, Aninda J. Bhattacharyya, Tetrahedrite ($Cu_{12}Sb_4S_{13}$) ternary inorganic hole conductor for ambient processed stable perovskite solar cells, ACS Appl. Energy Mater. 1 (2018) 4227–4234, https://doi.org/10.1021/acsaem.8b00844.

[13] D.S. Prem Kumar, M. Ren, T. Osipowicz, R.C. Mallik, P. Malar, Tetrahedrite ($Cu_{12}Sb_4S_{13}$) thin films for photovoltaic and thermoelectric applications, Sol. Energy 174 (2018) 422–430, https://doi.org/10.1016/j.solener.2018.08.080.

[14] O. Dobrozhan, R. Pshenychnyi, O. Klymov, E. Zuñiga-Puelles, C. Martínez-Tomás, V. Muñoz-Sanjosé, R. Gumeniuk, A. Opanasyuk, Synthesis and characterization of nanostructured tetrahedrite and its composite with dielectric inclusions, Mater. Sci. Semicond. Process. 182 (2024) 108690, https://doi.org/10.1016/J.MSSP.2024.108690.

[15] O. Dobrozhan, P. Danylchenko, A. Novgorodtsev, A. Opanasyuk, Optical and recombination losses in $Cu_2ZnSn(S,Se)_4$-based thin-film solar cells with CdS, ZnSe, ZnS window and ITO, ZnO charge-collecting layers, J. Nanoelectron. Optoelectron. 13 (2018) 195–207, https://doi.org/10.1166/jno.2018.2192.

[16] M. Haghighi, M. Minbashi, N. Taghavinia, D.-H. Kim, S.M. Mahdavi, A.A. Kordbacheh, A modeling study on utilizing SnS_2 as the buffer layer of CZT(S, Se) solar cells, Sol. Energy 167 (2018) 165–171, https://doi.org/10.1016/j.solener.2018.04.010.

[17] B.K. Meyer, Band structure, in: Zinc Oxide: from Fundamental Properties Towards Novel Applications, Springer, Berlin, Heidelberg, 2010, pp. 77–94, https://doi.org/10.1007/978-3-642-10577-7_4.

[18] X. Zhang, H. Ma, J. Ma, F. Zong, H. Xiao, F. Ji, Effect of annealing temperature on properties of $Mg_xZn_{1-x}O$ thin films deposited by RF magnetron sputtering, Physica B 357 (2005) 428–432, https://doi.org/10.1016/J.PHYSB.2004.12.009.

[19] O. Dobrozhan, O. Klymov, S. Agouram, C. Martínez-Tomás, V. Muñoz-Sanjosé, A. Opanasyuk, Grain growth of ZnO nanocrystals synthesized in polyol medium with polyvinylpyrrolidone additives, Ceram. Int. 50 (2024) 6941–6949, https://doi.org/10.1016/J.CERAMINT.2023.12.043.

[20] O. Dobrozhan, I. Shelest, A. Stepanenko, D. Kurbatov, M. Yermakov, A. Čerškus, S. Plotnikov, A. Opanasyuk, Structure, substructure and chemical composition of ZnO nanocrystals and films deposited onto flexible substrates, Mater. Sci. Semicond. Process. 108 (2020) 104879, https://doi.org/10.1016/J.MSSP.2019.104879.

[21] F. Ghisani, K. Timmo, M. Altosaar, J. Raudoja, V. Mikli, M. Pilvet, M. Kauk-Kuusik, M. Grossberg, Synthesis and characterization of tetrahedrite $Cu_{10}Cd_2Sb_4S_{13}$ monograin material for photovoltaic application, Mater. Sci. Semicond. Process. 110 (2020) 104973, https://doi.org/10.1016/j.mssp.2020.104973.

[22] M. Dhankhar, O.P. Singh, V.N. Singh, Physical principles of losses in thin film solar cells and efficiency enhancement methods, Renew. Sustain. Energy Rev. 40 (2014) 214–223, https://doi.org/10.1016/j.rser.2014.07.163.

[23] M. Ivashchenko, A. Opanasyuk, I. Buryk, D. Kuzmin, Numerical simulation of SnS-based solar cells, J. Nano- Electron. Phys. 10 (2018) 1–6, https://doi.org/10.21272/jnep.10(3).03004.

[24] O. Diachenko, O. Dobrozhan, A. Opanasyuk, D. Kurbatov, V. Grynenko, S. Plotnikov, Efficiency modeling of solar cells based on the n-$Zn_{1-x}Mg_xO$/p-SnS heterojunction, J. Nano- Electron. Phys. 11 (2019) 1–7, https://doi.org/10.21272/jnep.11(3).03024.

[25] O. Diachenko, O. Dobrozhan, A. Opanasyuk, M. Ivashchenko, T. Protasova, D. Kurbatov, A. Čerškus, The influence of optical and recombination losses on the efficiency of thin-film solar cells with a copper oxide absorber layer, Superlattice. Microst. 122 (2018) 476–485, https://doi.org/10.1016/j.spmi.2018.06.063.

[26] O. Diachenko, A. Opanasyuk, I. Buryk, D. Kuzmin, A. Čerškus, O. Shapovalov, S. Plotnikov, I. Gryshko, A numerical simulation of solar cells based on the CuO and Cu_2O absorber layers with ZnMgO window layer, Mater. Sci. Eng. B 300 (2024) 117133, https://doi.org/10.1016/j.mseb.2023.117133.

[27] S. Kakherskyi, O. Diachenko, N. Opanasyuk, A. Opanasyuk, Optical losses in glass/ITO(ZnO)/CdS/$Cu_2ZnSn(S_xSe_{1-x})_4$ solar cells with different kesterite composition, Trans. Electr. Electron. Mater. 23 (2022) 552–562, https://doi.org/10.1007/s42341-022-00387-8.

[28] M.K.A. Mohammed, Boosting efficiency in carbon nanotube-integrated perovskite photovoltaics, Langmuir 40 (2024) 27114–27125, https://doi.org/10.1021/acs.langmuir.4c04679.

[29] M.K.A. Mohammed, A.K. Al-Mousoi, S. Singh, A. Kumar, M.K. Hossain, S.Q. Salih, P. Sasikumar, R. Pandey, A.A. Yadav, Z.M. Yaseen, Improving the performance of perovskite solar cells with carbon nanotubes as a hole transport layer, Opt. Mater. 138 (2023) 113702, https://doi.org/10.1016/j.optmat.2023.113702.

[30] M. Aliaghayee, Optimization of the perovskite solar cell design with layer thickness engineering for improving the photovoltaic response using SCAPS-1D, J. Electron. Mater. 52 (2023) 2475–2491, https://doi.org/10.1007/s11664-022-10203-x.

[31] A.K. Al-Mousoi, M.K.A. Mohammed, R. Pandey, J. Madan, D. Dastan, G. Ravi, P. Sakthivel, G. Anandha babu, Simulation and analysis of lead-free perovskite solar cells incorporating cerium oxide as electron transporting layer, RSC Adv. 12 (2022) 32365–32373, https://doi.org/10.1039/D2RA05957F.
[32] S. Rühle, Tabulated values of the Shockley–Queisser limit for single junction solar cells, Sol. Energy 130 (2016) 139–147, https://doi.org/10.1016/j.solener.2016.02.015.
[33] N. Shah, A.A. Shah, P.K. Leung, S. Khan, K. Sun, X. Zhu, Q. Liao, A review of third generation solar cells, Processes 11 (2023) 1852, https://doi.org/10.3390/pr11061852.
[34] M. Cellura, L.Q. Luu, F. Guarino, S. Longo, A review on life cycle environmental impacts of emerging solar cells, Sci. Total Environ. 908 (2023) 168019, https://doi.org/10.1016/j.scitotenv.2023.168019.
[35] L.A. Kosyachenko, E.V. Grushko, T.I. Mikityuk, Absorptivity of semiconductors used in the production of solar cell panels, Semiconductors 46 (2012) 466–470, https://doi.org/10.1134/S1063782612040124/METRICS.
[36] International Organization for Standardization, Solar Energy — Reference Solar Spectral Irradiance at the Ground at Different Receiving Conditions — Part 1: Direct Normal and Hemispherical Solar Irradiance for Air Mass, 1.5, 2022. ISO 9845-1.
[37] T. Rath, A.J. MacLachlan, M.D. Brown, S.A. Haque, Structural, optical and charge generation properties of chalcostibite and tetrahedrite copper antimony sulfide thin films prepared from metal xanthates, J. Mater. Chem. A 3 (2015) 24155–24162, https://doi.org/10.1039/C5TA05777A.
[38] R. Scheer, H.-W. Schock, Introduction, in: Chalcogenide Photovoltaics, Wiley, Weinheim, 2011, pp. 1–8, https://doi.org/10.1002/9783527633708.ch1.
[39] O. Dobrozhan, M. Baláž, S. Vorobiov, P. Baláž, A. Opanasyuk, Morphological, structural, optical properties and chemical composition of flexible Cu_2ZnSnS_4 thin films obtained by ink-jet printing of polyol-mediated nanocrystals, J. Alloys Compd. 842 (2020) 155883, https://doi.org/10.1016/J.JALLCOM.2020.155883.
[40] H.A. Mohamed, Dependence of efficiency of thin-film CdS/CdTe solar cell on optical and recombination losses, J. Appl. Phys. 113 (2013) 93105, https://doi.org/10.1063/1.4794201.
[41] L. Kosyachenko, E. Grushko, X. Mathew, Quantitative assessment of optical losses in thin-film CdS/CdTe solar cells, Sol. Energy Mater. Sol. Cells 96 (2012) 231–237, https://doi.org/10.1016/j.solmat.2011.09.063.
[42] A. Bikowski, The relation between the deposition process and the structural, electronic, and transport properties of magnetron sputtered doped ZnO and $Zn_{1-x}Mg_xO$ films, Humboldt-Universität zu Berlin. https://doi.org/10.18452/16994, 2014.
[43] S. Kasap, Optoelectronics & Photonics: Principles & Practices, second ed., Pearson, Boston, 2013.
[44] S. Adachi, Handbook on Physical Properties of Semiconductors, Kluwer Academic Publishers, Boston, 2004.
[45] L. Kosyachenko, T. Toyama, Current–voltage characteristics and quantum efficiency spectra of efficient thin-film CdS/CdTe solar cells, Sol. Energy Mater. Sol. Cells 120 (2014) 512–520, https://doi.org/10.1016/j.solmat.2013.09.032.
[46] L. Kosyachenko, Problems of efficiency of photoelectric conversion in thin-film CdS/CdTe solar cells, Semiconductors 40 (2006) 710–727, https://doi.org/10.1134/s1063782606060182.
[47] R. Ding, C. Xu, B. Gu, Z. Shi, H. Wang, L. Ba, Z. Xiao, Effects of Mg incorporation on microstructure and optical properties of ZnO thin films prepared by sol-gel method, J. Mater. Sci. Technol. 26 (2010) 601–604, https://doi.org/10.1016/S1005-0302(10)60092-8.
[48] H. Krysova, V. Mansfeldova, H. Tarabkova, A. Pisarikova, Z. Hubicka, L. Kavan, High-quality dense ZnO thin films: work function and photo/electrochemical properties, J. Solid State Electrochem. 28 (2024) 2531–2546, https://doi.org/10.1007/s10008-023-05766-6.
[49] S.M. Sze, M.-K. Lee, Semiconductor Devices: Physics and Technology, third ed., Wiley, New York, 2012.
[50] R. Chetty, A. Bali, R.C. Mallik, Tetrahedrites as thermoelectric materials: an overview, J. Mater. Chem. C 3 (2015) 12364–12378, https://doi.org/10.1039/c5tc02537k.
[51] M. Balkanski, R.F. Wallis, Semiconductor Physics and Applications, Oxford University Press, Oxford, 2000, https://doi.org/10.1093/oso/9780198517412.001.0001.
[52] W. Spear, J. Mort, Electron and hole transport in CdS crystals, Proc. Phys. Soc. 81 (1963) 130–140, https://doi.org/10.1088/0370-1328/81/1/319.
[53] N. Basov, Exciton and Domain Luminescence of Semiconductors, Springer, New York, 2012, https://doi.org/10.1007/978-1-4615-8573-2.
[54] D. Chi, S. Huang, S. Yue, K. Liu, S. Lu, Z. Wang, S. Qu, Z. Wang, Ultra-thin ZnO film as an electron transport layer for realizing the high efficiency of organic solar cells, RSC Adv. 7 (2017) 14694–14700, https://doi.org/10.1039/c6ra27543e.
[55] T. Ahamed, F. Rayhan, I. Rahaman, M.H. Rahman, M.M. Hasan Bappy, T. Ahammed, S. Ghosh, Optimization of buffer layers for CZTSSe solar cells through advanced numerical modelling, J. Phys. Chem. Solid. 204 (2025) 112744, https://doi.org/10.1016/j.jpcs.2025.112744.
[56] H. Jalali, A.A. Orouji, I. Gharibshahian, Controlled conduction band offset in Sb2Se3 solar cell through introduction of (Zn,Sn)O buffer layer to improve photovoltaic performance: a simulation study, Sol. Energy Mater. Sol. Cells 260 (2023) 112492, https://doi.org/10.1016/j.solmat.2023.112492.
[57] M. Moustafa, Z. Abu Waar, S. Yasin, Optimizing solar performance of CFTSe-based solar cells using $MoSe_2$ as an innovative buffer layers, Sci. Rep. 15 (2025) 614, https://doi.org/10.1038/s41598-024-82309-7.
[58] R. Hosen, S. Sikder, MdS. Uddin, MdM. Haque, H. Mamur, M.R.A. Bhuiyan, Effect of various layers on improving the photovoltaic efficiency of Al/ZnO/CdS/CdTe/Cu2O/Ni solar cells, J. Alloys Metall. Syst. 4 (2023) 100041, https://doi.org/10.1016/j.jalmes.2023.100041.
[59] L. Sun, W. Wang, L. Hao, A. Raza, Y. Zhao, Z. Tang, G. Zhi, H. Yao, Effect of TiN diffusion barrier layer on residual stress and carrier transport in flexible CZTSSe solar cells, Ceram. Int. 48 (2022) 19891–19899, https://doi.org/10.1016/j.ceramint.2022.03.264.
[60] R. Wuerz, W. Hempel, P. Jackson, Diffusion of Rb in polycrystalline $Cu(In,Ga)Se_2$ layers and effect of Rb on solar cell parameters of $Cu(In,Ga)Se_2$ thin-film solar cells, J. Appl. Phys. 124 (2018), https://doi.org/10.1063/1.5044629.
[61] L. Wang, B. Yang, Z. Xia, M. Leng, Y. Zhou, D.-J. Xue, J. Zhong, L. Gao, H. Song, J. Tang, Synthesis and characterization of hydrazine solution processed $Cu_{12}Sb_4S_{13}$ film, Sol. Energy Mater. Sol. Cells 144 (2016) 33–39, https://doi.org/10.1016/j.solmat.2015.08.016.
[62] M.S. Kim, J.H. Lee, M.K. Kwak, Review: surface texturing methods for solar cell efficiency enhancement, Int. J. Precis. Eng. Manuf. 21 (2020) 1389–1398, https://doi.org/10.1007/s12541-020-00337-5.
[63] R. Sagar, A. Rao, RF sputtered metal oxide layers as ARCs to improve photovoltaic performance of commercial monocrystalline solar cell, Opt. Mater. 150 (2024) 115276, https://doi.org/10.1016/J.OPTMAT.2024.115276.
[64] C. Yan, J. Huang, K. Sun, S. Johnston, Y. Zhang, H. Sun, A. Pu, M. He, F. Liu, K. Eder, L. Yang, J.M. Cairney, N.J. Ekins-Daukes, Z. Hameiri, J.A. Stride, S. Chen, M.A. Green, X. Hao, Cu_2ZnSnS_4 solar cells with over 10% power conversion efficiency enabled by heterojunction heat treatment, Nat. Energy 3 (2018) 764–772, https://doi.org/10.1038/s41560-018-0206-0.
[65] A.W. Welch, L.L. Baranowski, H. Peng, H. Hempel, R. Eichberger, T. Unold, S. Lany, C. Wolden, A. Zakutayev, Trade-offs in thin film solar cells with layered chalcostibite photovoltaic absorbers, Adv. Energy Mater. 7 (2017), https://doi.org/10.1002/aenm.201601935.
[66] S. Banu, S.J. Ahn, S.K. Ahn, K. Yoon, A. Cho, Fabrication and characterization of cost-efficient $CuSbS_2$ thin film solar cells using hybrid inks, Sol. Energy Mater. Sol. Cells 151 (2016) 14–23, https://doi.org/10.1016/j.solmat.2016.02.013.
[67] O. Dobrozhan, R. Pshenychnyi, M. Yermakov, B. Boiko, S. Vorobiov, V. Tkáč, A. Opanasyuk, Structural, substructural, magnetic, and electrical properties of Ti-substituted tetrahedrites with enhanced thermoelectric performance, Mater. Sci. Semicond. Process. 193 (2025) 109520, https://doi.org/10.1016/J.MSSP.2025.109520.
[68] O. Dobrozhan, R. Pshenychnyi, O. Klymov, M. Yermakov, B. Boiko, S. Agouram, V. Muñoz-Sanjosé, A. Opanasyuk, Enhancing the thermoelectric power factor of metal/tetrahedrite nanocomposites via phase boundary engineering, Mater. Sci. Semicond. Process. 194 (2025) 109548, https://doi.org/10.1016/J.MSSP.2025.109548.